Chemical Engineering Journal 517 (2025) 164281

Contents lists available at ScienceDirect

Chemical Engineering Journal

journal homepage: www.elsevier.com/locate/cej

Structural optimization of TiO_2 supported IrO_2 catalyst for proton exchange membrane water electrolysis

Darius Hoffmeister [a,b,*], Selina Finger [a,b], Ramesh Pokhrel [a,b], Andreas Körner [a,b], Birk Fritsch [a], Simon Thiele [a,b], Andreas Hutzler [a], Chuyen van Pham [a,*]

[a] Helmholtz-Institute Erlangen-Nürnberg for Renewable Energy (IET-2), Forschungszentrum Jülich, Cauerstr. 1, 91058 Erlangen, Germany
[b] Department Chemical and Biological Engineering, Friedrich-Alexander-Universität Erlangen-Nürnberg, Egerlandstr. 3, 91058 Erlangen, Germany

ABSTRACT

Reducing the iridium loading in proton exchange membrane water electrolysis (PEMWE) is essential, and catalysts with a low iridium content are one viable approach to reach this goal. This study investigates a series of TiO_2 supported IrO_2 catalysts with three different TiO_2 support-particle sizes (3, 14, and 56 $m^2\ g^{-1}$) and three different iridium oxide contents (30, 50, and 70 wt%). We demonstrate that, for optimal iridium utilization, the nominal IrO_2 shell thickness should be maximized, which is readily achieved by employing low-surface area supports. Following this strategy, a TiO_2@IrO_2 catalyst with 50 wt% IrO_2 is designed, whose single-cell performance exceeds a commercial reference catalyst (88 wt% IrO_2) by 43 mV at 2 A cm^{-2} at a low iridium loading of 0.1 $mg_{Ir}\ cm^{-2}$. Furthermore, we find a strong correlation between powder conductivity measurements and single-cell high frequency resistance, underlining the importance of catalyst conductivity.

1. Introduction

Proton exchange membrane water electrolysis (PEMWE) is a promising way of producing green hydrogen. Even though the technology has many advantages, such as high current densities and fast load following, the scarcity of the noble metal iridium seriously hampers the large-scale implementation of the technology. Iridium is the main catalyst material for the anodic catalyst for the oxygen evolution reaction (OER). As previously shown, the iridium loading must be substantially decreased [1,2]. The main reason for choosing the rare element iridium is its high corrosion resistance in the harsh environment at the PEMWE anode, namely high potentials, low pH, and elevated temperature. Unfortunately, other catalyst materials, such as ruthenium oxides, ruthenium-iridium mixed oxides, or non-noble metals, usually show high dissolution rates and fast degradation under these conditions [3–5]. Consequently, PEMWE will be operated with iridium-based catalysts, at least in the near and mid-term future. However, current iridium loadings of 1–3 $mg_{Ir}\ cm^{-2}$ are not feasible for large-scale implementation. Instead, loadings $< 0.5\ mg_{Ir}\ cm^{-2}$, preferably $< 0.1\ mg_{Ir}\ cm^{-2}$, should be aimed for [2,6–9]. This poses a serious challenge to currently commercially available catalysts: As these often contain a high iridium content of ≥ 75 wt%, the resulting catalyst layer (CL) at a low iridium loading becomes too thin. This leads to partially disconnected CLs due to crack formation or inhomogeneous layer structures [6,10–12]. Hence, to produce sufficiently thick CLs ($> 2\ \mu m$) [6] at low iridium loadings ($< 0.5\ mg_{Ir}\ cm^{-2}$), the iridium content in the catalyst powder should be reduced.

Reducing the iridium content in the catalyst powder is usually achieved by introducing support particles. However, these support particles experience the same harsh conditions as the active catalyst material, so the choice of stable support materials is limited. While conductive materials such as tantalum–doped TiO_2 [13] and antimony-doped tin oxide (ATO) [14–16] are being investigated as potential support particles for iridium-based catalysts, their long-term stability is often insufficient or at least questionable [17]. Titanium dioxide (TiO_2) has been successfully used as a stable support material in recent years [18–21]. However, being a wide-bandgap semiconductor, the conductivity of TiO_2 in PEMWE application is negligible [2,13]. Therefore, the electric conduction must be provided solely by the iridium phase. A core–shell structure with the iridium (oxide) shell covering the TiO_2 support is usually aimed for ensure interparticle conduction pathways [9,19,21]. This core–shell strategy requires a delicate balance between reducing the iridium content on the one hand and maintaining sufficient electrical percolation on the other hand. The question arises whether the electrical

---

* Corresponding authors at: Helmholtz-Institute Erlangen-Nürnberg for Renewable Energy (IET-2), Forschungszentrum Jülich, Cauerstr. 1, 91058 Erlangen, Germany.

E-mail addresses: d.hoffmeister@fz-juelich.de (D. Hoffmeister), s.finger@fz-juelich.de (S. Finger), rameshpokhrel5@gmail.com (R. Pokhrel), a.koerner@fz-juelich.de (A. Körner), b.fritsch@fz-juelich.de (B. Fritsch), si.thiele@fz-juelich.de (S. Thiele), a.hutzler@fz-juelich.de (A. Hutzler), c.pham@fz-juelich.de (C. van Pham).

https://doi.org/10.1016/j.cej.2025.164281
Received 24 January 2025; Received in revised form 15 April 2025; Accepted 28 May 2025

percolation is directly linked to the iridium (oxide) shell thickness. If yes, then optimizing the shell thickness aspires to maximize the electrochemical performance at the lowest possible iridium content. Additionally, one question that has not been answered so far is: How much iridium is needed to form a percolating shell?

Geometric considerations show that the required iridium content to reach a given shell thickness scales with the specific surface area of the support particles [21,22]. Consequently, a lower support particle surface area requires less iridium to reach the same shell thickness. Thus, the iridium (oxide) shell thickness can be tuned by the support particle surface area and the iridium content. This study systematically investigates the relationship between TiO_2 surface area, iridium content, and IrO_2 shell thickness and links these parameters to the electrocatalytic properties. In doing so, we aim to deepen the understanding of the structure–property relationships for these types of TiO_2@IrO_2 catalysts while at the same time employing stable materials.

We use a previously developed, surface-charge-assisted synthesis method for producing TiO_2-supported IrO_2 catalysts with an IrO_2 particle shell [9] to investigate a matrix of three different TiO_2 support-particle sizes and three different IrO_2 contents. Employing geometric considerations, a nominal IrO_2 shell thickness can be calculated for each of these nine catalysts. In this context, we investigate if a nominal IrO_2 shell thickness can be used as a general descriptor to optimize the structure and the electrocatalytic performance of TiO_2@IrO_2 catalysts. Therefore, extensive physical characterizations, including scanning transmission electron microscopy (STEM) with energy-dispersive X-ray spectroscopy (EDXS), N_2 physisorption, X-ray diffraction (XRD), X-ray fluorescence (XRF), and powder conductivity measurements were performed to complement the electrochemical characterizations on a rotating disk electrode (RDE) and in low-loaded CLs in a 5 cm^2 PEMWE single-cell.

Furthermore, we use this structural study to evaluate how well the results of the employed pre-testing methods correlate with the performance of a single-cell PEM water electrolyzer.

2. Experimental

2.1. TiO_2 supported IrO_2 catalyst synthesis

The synthesis of the nine different TiO_2 supported IrO_2 catalysts with an IrO_2 particle shell (TiO_2@IrO_2) is based on a surface-charge assisted pyrolysis described and analyzed in detail in our previous work [9]. In short, by using acetic acid to adjust the pH of the precursor solution to pH < 6, a positive zeta potential is induced on the TiO_2 particles, which attracts the negatively charged $[IrCl_6]^{2-}$ ions. Upon evaporating the solvents, this precursor forms a shell around the TiO_2 particles (TiO_2@H_2IrCl_6) due to the electrostatic interaction. Lastly, the precursor shell is transformed into an iridium oxide particle shell (TiO_2@IrO_2) in a pyrolysis step at 500 °C under an oxygen atmosphere.

Exemplarily, for a catalyst with 50 wt% IrO_2, 0.224 g TiO_2 and 0.479 g H_2IrCl_6 xH_2O ($>$ 99.9 % trace metals basis, Sigma Aldrich) were mixed with 10 mL ethanol (absolute for analysis, $\geq$ 99.9 %, Merck KGaA), 20 μL acetic acid (glacial, $\geq$ 99.7 %, Sigma Aldrich) and 10 μL deionized (DI) water (18.2 MΩ cm) in a round bottom flask. After 15 min in an ultrasonic bath, the reaction solution was heated to 105 °C under constant stirring, and the flask was opened to allow the evaporation of the solvent. The resulting solid phase was transferred to a tube furnace and heated to 500 °C at a rate of 5 K min^{-1} and an oxygen flow of 100 mL min^{-1}. The temperature was held at 500 °C for 30 min and subsequently allowed to cool down naturally. Finally, the obtained powder was ground in an agate mortar for 20 min to obtain a fine TiO_2@IrO_2 powder.

In this work, we obtain different IrO_2 shell thicknesses by varying the IrO_2 content and the TiO_2 specific surface area. The nominal IrO_2 shell thicknesses are calculated based on the assumption that all the iridium precursor is deposited as a homogeneous layer of IrO_2 on the surface area of support particles (cf. section 3.1 for details on the calculation). Three different TiO_2 particles were used as support: TiO_2 with a specific surface area of 3 m^2 g^{-1} (TiO_2 $<$ 5 μm rutile, $\geq$ 99.9 % trace metals basis, Sigma Aldrich), TiO_2 with a specific surface area of 14 m^2 g^{-1} (TiO_2 $<$ 500 nm, rutile, $\geq$ 99.9 % trace metals basis, American Elements), and TiO_2 with a specific surface area of 56 m^2 g^{-1} (TiO_2 $\approx$ 21 nm, $\geq$ 99.5 % trace metals basis, Sigma Aldrich). The reported specific surface areas were measured *via* N_2 physisorption. Three different catalysts with IrO_2 contents of 30, 50, and 70 wt% were synthesized for each support particle type, resulting in a matrix of nine different catalysts.

Generally, this synthesis method shows high reproducibility, with up to five synthesis batches showing nearly identical activities, as shown in the RDE measurements in Fig. S1. For potential future scale-up of the synthesis method, the time between mixing the chemicals and complete solvent evaporation should be kept as low as possible, preferably less than 1 h. Our observations suggest that prolonged standing times (several hours) of the iridium precursor solution combined with titanium oxide can result in morphologic changes of the TiO_2. This is likely due to the high concentration and strong acidic properties of the chloroiridic acid.

2.2. Catalyst layer fabrication

In our previous work, the TiO_2@IrO_2 catalyst outperformed commercial catalysts in a porous transport electrode (PTE) configuration [9]. Here, the performance of various TiO_2@IrO_2 catalysts is tested in a half-catalyst coated membrane (hCCM) configuration by coating the anodic catalyst layer (CL) directly onto the membrane.

The fabrication of hCCMs with an active area of 5 cm^2 is achieved by spray coating the catalyst ink directly onto a Nafion NR212 membrane (dry thickness ~51 μm, Chemours). A 1:1 wt ratio of DI water and isopropanol ($>$ 99.8 %, Sigma-Aldrich) was used as solvents for the catalyst ink, as well as a solid content of 1 wt%, consisting of 98 wt% of the respective catalyst powder and 2 wt% Nafion (using Nafion^{TM} D2021 ionomer dispersion, Chemours), as described by Bühler et al. [23] The actual Nafion content in the spraycoated layers was measured to be ~3 wt%, as determined *via* thermogravimetric analysis (TGA; Fig. S2). Before the spray coating, the catalyst inks were sonicated with an ultrasonic horn (Hielscher UIS250 L) for 30 min at 40 W with 20 % breaks (0.8 s on, 0.2 s off) in an ice bath. For optimal dispersion, the catalyst inks were continuously stirred in the syringe of the spray coater during the coating process. The catalyst inks were sprayed with an ultrasonic spray coater (Exacta Coat, Sono-Tek) with an AccuMist nozzle (48 kHz) onto the membrane that was kept flat on a heated glass plate set to 80 °C. A meander-shaped path was sprayed with an ink flow rate of 0.45 ml min^{-1}, a nozzle speed of 140 mm s^{-1}, and a shaping air pressure of 0.6 kPa. To determine the loadings of the hCCMs, a 5 cm^2 carbon paper reference was spraycoated simultaneously with each hCCM and repeatedly weighed on a microbalance (Sartorius ME 36S) until the desired loadings of 0.40 and 0.10 mg_{Ir} cm^{-2} were reached within an accuracy of $\pm$0.01 mg_{Ir} cm^{-2}.

For the cathode, a commercially available carbon cloth gas diffusion electrode (GDE) with a loading of 0.5 mg_{Pt} cm^{-2} (SL–GDE, 60 wt% Pt/C Vulcan, FuelCellsEtc) was used for all single-cell tests.

2.3. Physical characterization

2.3.1. Transmission electron microscopy (TEM)

TEM samples were prepared by dipping a TEM grid (Lacey carbon on Ni grid, TedPella) into a catalyst dispersion in H_2O and isopropanol. For HAADF-STEM imaging and EDX spectrum imaging, a Talos F200i from Thermo Fisher Scientific equipped with a Schottky emitter (X-FEG) and a Dual Bruker XFlash 6 T-100 EDS detector was used with a primary electron energy of 200 keV. Micrographs were processed using Velox (v. 3.9.0).

2.3.2. N_2 physisorption

N_2 physisorption was employed to determine the specific surface area of the catalyst powder samples. Before measuring, all samples were degassed for 24 h at 423 K and <0.05 mbar. The N_2 physisorption adsorption isotherm was measured at 77 K with a Micromeritics TriStar II Plus and evaluated using the Brunauer-Emmett-Teller (BET) method [24] at partial pressures between 0.1 and 0.5 p/p_0.

2.3.3. XRD

To determine the crystal phase and crystallite size of the $TiO_2@IrO_2$ catalyst, representatively, one of the synthesized samples (50 wt% IrO_2, 3 $m^2\,g^{-1}$ TiO_2) was measured in a Rigaku Smartlab SE with a Cu Kα source (8047.8 eV). Rietveld refinement was performed on the obtained diffractogram with the software Profex (v. 5.3.0).[25] For TiO_2 rutile and anatase, PDF #04-003-0648 and PDF #04-007-0701 from the International Centre for Diffraction Data (ICDD) database were used, respectively. For IrO_2 rutile, mp-2723 from The Materials Project database was used [26].

2.3.4. XRF

To determine the iridium content of the synthesized $TiO_2@IrO_2$ catalysts, representatively, three of the synthesized samples (30, 50, and 70 wt% IrO_2, on 3 $m^2\,g^{-1}$ TiO_2) were measured in a Bruker M4 Tornado with a rhodium source at a voltage of 50 kV. Twenty spots were measured on each powder sample, and the ratio of IrO_2 to TiO_2 was averaged to determine the iridium oxide content of the three different catalysts.

2.3.5. Thermogravimetric analysis (TGA)

TGA was used to determine the ionomer content in the spraycoated CLs of the reference catalyst (Umicore Elyst Ir75 0480) and the best-performing $TiO_2@IrO_2$ catalyst (50 wt% IrO_2, 3 $m^2\,g^{-1}$ TiO_2). For this, the spraycoated layers were scratched off a PTFE substrate and subsequently measured. The pure catalysts were additionally measured as a reference so that the difference, which represents the ionomer content, could be calculated. The following measurement protocol was performed with a Perkin Elmer TGA 8000: Under a constant flow of synthetic air, first, the sample was held at 110 °C for 60 min to allow the evaporation of water, followed by heating to 800 °C at a rate of 5 $K\,min^{-1}$. The mass loss difference was averaged between 450 and 800 °C, revealing a Nafion content of ~3 wt% in the spraycoated layers, as shown in Fig. S2.

2.3.6. Powder conductivity

The powder conductivity measurements were performed in a 3D-printed setup [27], described in detail in our previous work [12]. Shortly, 20 mg of catalyst powder was compressed with 3 MPa. The compression was precisely controlled by a tensile tester in compression mode (Shimadzu EZ-SX), which simultaneously enabled a thickness measurement of the compressed powder. Using a van der Pauw configuration, four embedded copper electrodes were used to determine the powder conductivity. Current and voltages were measured with a four-point probe's built-in source measure unit (Ossila B. V., Four-Point Probe T2001A3).

2.3.7. In-plane conductivity

The in-plane conductivity of the catalyst layers was measured on the hCCMs after PEMWE single-cell testing to avoid influencing the electrochemical measurements. A four-point probe (Ossila B. V., Four-Point Probe T2001A3) was used for the measurement. All measurements were performed three separate times on two dried hCCMs for each catalyst layer, resulting in six measurements per catalyst.

2.4. Electrochemical characterization

2.4.1. RDE

All RDE measurements were performed at room temperature in 0.1 M perchloric acid (prepared from 70 % $HClO_4$, EMSURE®, Sigma Aldrich), which was purged with argon for 30 min before the measurement and blanketed with argon during the measurement. A mirror-polished gold electrode with an area of 0.196 cm^2 served as the substrate for the catalyst coating, and a reversible hydrogen electrode (RHE Hydroflex, Gaskatel) and a Pt wire electrode (99.99 %, Pine Research) were used as a reference and counter electrode, respectively.

For the coating, a catalyst ink with a solvent ratio of 3:1 vol ratio of DI water (18.2 MΩ cm) and isopropanol (> 99.8 %, Sigma-Aldrich) was prepared. The amount of catalyst was chosen so that an ink volume of 20 μL (drop cast as 2 x 10 μL) resulted in a coating with a loading of 50 $\mu g_{Ir}\,cm^{-2}$, with catalyst masses between 5.1 and 15.3 mg, depending on the iridium content of the catalyst. The amount of ionomer dispersion (Nafion^{TM} D520, Chemours) was adjusted to yield a Nafion solid content of 10 wt%. For a homogeneous dispersion, the catalyst inks were sonicated for 15 min in an ultrasonic bath before drop casting.

During the RDE measurement, the working electrode was rotated at 1600 rpm in a commercial RDE setup (Pine Research, WaveVortex 10 Rotator). The measurement consisted of two techniques: First, five cyclic voltammograms at different scan rates (5, 10, 25, 50, and 100 $mV\,s^{-1}$) were recorded in the non-faradaic region between 1.18 and 1.28 V vs. RHE. Secondly, the OER activity was assessed by performing three consecutive linear sweep voltammograms in the potential range from 1.1 to 1.8 V vs. RHE at a scan rate of 5 $mV\,s^{-1}$. Only the last LSV was taken for OER evaluation. All measurements were performed three times on separate coatings for each catalyst ink. An approximate 80 % iR-correction was applied during all measurements as on-the-fly compensation using the built-in hardware in the potentiostat (Nordic Electrochemistry, ECi 210). The remaining resistance (~5 Ω) was constantly measured and subtracted from the data to yield the iR–free potentials.

2.4.2. PEMWE single-cell testing

Single-cell testing was performed on a commercial test system (600 Electrolyzer Test System, Scribner LLC) equipped with a potentiostat with a current booster (BioLogic VSP-300). An in-house designed cell fixture with an active area of 5 cm^2 (adapted from previous reports [28]) was used. On the anode side, an uncoated titanium fiber porous transport layer (PTL) with a thickness of 250 μm (2GDL10-0.25, Bekaert) and one of the spray-coated anode catalyst layers (as hCCM on Nafion NR212) were used. The three best catalysts from pre-testing and a commercial IrO_2/TiO_2 reference catalyst (Umicore Elyst Ir75 0480) were tested at a loading of 0.4 ± 0.01 $mg_{Ir}\,cm^{-2}$, and the two best catalysts from these single-cell tests were additionally tested at a loading of 0.1 ± 0.01 $mg_{Ir}\,cm^{-2}$. On the cathode side, a commercially available carbon cloth gas diffusion electrode (GDE) with a loading of 0.5 $mg_{Pt}\,cm^{-2}$ (SL–GDE, 60 wt% Pt/C Vulcan, FuelCellsEtc) was employed for all single-cell tests. Gasket thicknesses were chosen to compress the carbon GDEs in a range of 24.3 ± 1.2 %.

During testing, the anode side was flushed with 100 $mL\,min^{-1}$ DI water that had been purged for 10 min with N_2 prior to testing to remove any dissolved CO_2. The anode feed and the cell hardware were heated to 80 °C, and the temperature was kept constant during testing. The cathode was operated in a dry state, and only the venting line behind the cathode outlet was purged with nitrogen for safety reasons. 30 min after the cell temperature had reached 80 °C, the electrochemical testing was started.

The electrochemical protocol started with a test for an electrical short by holding the potential at 1 V for 1 min, followed by a conditioning step of 1 $A\,cm^{-2}$ for 30 min.

Subsequently, three polarization curves were acquired at current densities between 0.01 and 4 $A\,cm^{-2}$. Each current density was held for 5 min to ensure a steady-state condition, and the last 30 data points

(= 15 s) of the current density hold were averaged for analysis. After each point of the polarization curve, galvanostatic electrochemical impedance spectroscopy (EIS) was measured in a frequency range from 100 kHz to 500 mHz. To ensure a linear system response and a good signal-to-noise ratio, the perturbation of each AC current was chosen to be $\leq$ 10 % of the AC current but not smaller than 20 mA. Of the three polarization curves recorded, only the last one was taken for analysis. Due to the high reproducibility of the polarization curves and the apparent differences between catalyst performances, all single-cell tests were performed two times with pristine materials.

For the PEMWE stability test, two different single cells containing the best-performing synthesized catalyst (50 wt% IrO_2 on 3 $m^2\,g^{-1}$ TiO_2 support) and the reference catalyst, respectively, were tested at a loading of 0.4 $mg_{Ir}\,cm^{-2}$. After the same conditioning protocol as described above, the current density was held at 2 $A\,cm^{-2}$ for 200 h. Additionally, polarization curves were acquired at the beginning of test, after 100 h, and the end of test. Platinum-coated Ti PTLs (250 μm 'Currento', Bekaert) were used for stability testing. Apart from that, all other materials and testing parameters were identical to the other PEMWE single-cell tests.

2.4.3. HFR and Tafel fitting

An in-house developed Python routine was used to fit the HFRs from the electrochemical impedance measurements. The details of the fitting procedure are reported in our previous work [12]. Shortly, an equivalent circuit model consisting of an inductance, a resistor, and a transmission line model in series was used to fit the electrochemical impedance measurements at each measured current density in a frequency interval of 60–1 kHz. A flow chart of the Python routine is shown in Fig. S3.

The Tafel slopes were fitted into the semi-logarithmic representation of the HFR-free polarization curves in a current density range of 0.005–0.05 $A\,cm^{-2}$ using a linear regression.

3. Results and discussion

3.1. Calculation of the IrO_2 shell thickness

In this study, a previously developed synthesis method [9] is used to synthesize nine different TiO_2 supported IrO_2 catalysts with an IrO_2 particle shell (TiO_2@IrO_2) for investigating a matrix of three different TiO_2 support particle sizes (specific surface areas of 3, 14 and 56 $m^2\,g^{-1}$ as determined via N_2 physisorption measurements) and three different iridium oxide contents (30, 50, and 70 wt%). A nominal IrO_2 shell thickness can be calculated for each of these nine supported catalysts, which will be explained in the following section.

From the measured specific surface areas of the TiO_2 supports, the average TiO_2 particle sizes can be calculated assuming non-porous and monodisperse spheres (see Supplementary Material for derivation):

$$d_{TiO_2} = \frac{6}{A_{BET} \bullet \rho_{TiO_2}} \tag{1}$$

where d_{TiO2} is the diameter of the TiO_2 particles, A_{BET} is the specific surface area of the TiO_2 particles as determined via N_2 physisorption measurements, and ρ_{TiO_2} is the density of rutile TiO_2 (4.23 $g\,cm^{-3}$) [29].

Table 1 lists the measured specific surface areas and the calculated average particle sizes of the three TiO_2 support particles used in this study. The specific surface areas and the average particle sizes differ by about a factor of four between each type of support. Thus, a significant difference in the catalyst morphology is expected.

Table 1
Measured specific surface areas and corresponding calculated average particle sizes of the three different TiO2 support particles used in this work.

Nominal TiO_2 particle size/nm	Measured specific surface area/$m^2\,g^{-1}$	Calculated average TiO_2 particle size*/nm
21	55.5	25.6
<500	13.7	104
<5000	3.0	473

*Assuming non-porous and monodisperse spheres.

Using the average TiO_2 particle size, a nominal thickness for the IrO_2 shell of the TiO_2@IrO_2 catalysts can be calculated. By assuming a homogeneous, non-porous shell of IrO_2 and employing the equation for the volume of a hollow sphere (see Supplementary Material for derivation), the thickness of the IrO_2 shell equates to

$$t_{shell} = \sqrt[3]{r_{TiO_2}{}^3 + r_{TiO_2}{}^3 \bullet \frac{x}{100 - x} \bullet \frac{\rho_{TiO_2}}{\rho_{IrO_2}}} - r_{TiO_2} \tag{2}$$

where t_{shell} is the thickness of the shell, r_{TiO_2} is the calculated average radius of the TiO_2 particles, x is the IrO_2 weight content (as percentage), and ρ_{IrO2} is the density of rutile IrO_2 (11.66 $g\,cm^{-3}$) [30].

As schematically shown in Fig. 1a, the variations of the IrO_2 content and the TiO_2 surface area lead to different nominal thicknesses of the IrO_2 shell.

The nominal IrO_2 shell thickness is influenced by both the IrO_2 content and the TiO_2 surface area, as described by Eqs. (1) and (2). This relationship is visualized in the contour lines in Fig. 1b, where it is shown that thicker nominal shell thicknesses can be achieved by both increasing the IrO_2 content and decreasing the TiO_2 surface area. The nine synthesized catalysts in this study are marked in the plot, with their corresponding nominal shell thickness values listed in Table 2. Notably, the nominal shell thicknesses explored in this study span two orders of magnitude, from 0.6 nm (for 30 wt% IrO_2, 56 $m^2\,g^{-1}$ TiO_2) to 53.6 nm (for 70 wt% IrO_2, 3 $m^2\,g^{-1}$ TiO_2). Therefore, considerable differences in the electrochemical performance are expected.

The question arises as to whether this nominal shell thickness can be used as a general indicator for the performance of TiO_2@IrO_2 catalysts. This study investigates if there are universal trends in electrochemical performance depending on the nominal shell thickness.

3.2. Physical characterization

The iridium contents of the synthesized TiO_2@IrO_2 catalysts were validated *via* XRF measurements. As shown in Table S1, the measured values match the targeted values within the standard deviation.

The morphology of the different TiO_2@IrO_2 catalysts was analyzed in a series of high-angle annular dark field (HAADF)-STEM images and STEM-EDX spectrum images shown in Fig. 2 a–e and Figs. S4–S8. As demonstrated previously [9], the IrO_2 shell synthesized via this surface-charge assisted pyrolysis method is not completely dense but rather an agglomeration of many IrO_2 nanoparticles forming a shell-like structure. The measured shell thickness partially deviates from the nominal (calculated) shell thickness (Fig. S9), which we assume is due to the porous nature of the shell. Even though a dense and homogeneous IrO_2 shell thickness is the base to calculate what we denote as nominal shell thickness, the general concept and described trends remain unaffected. Additionally, this agglomeration-like shell provides a high IrO_2 surface area for the catalytic reaction even when support particles with a low specific surface area are used, as evidenced by measured specific surface areas between 12.1 and 47.5 $m^2\,g^{-1}$ for the nine TiO_2@IrO_2 catalysts (Fig. S10).

When the 3 $m^2\,g^{-1}$ TiO_2 support is used (Fig. 2a, b), a uniform core–shell morphology (with an IrO_2 particle shell) is achieved for iridium oxide contents of 30 and 50 wt%. This homogeneous core–shell structure, even at low iridium contents, is highly promising as it enables a high degree of percolation within the catalyst. This percolation is evidenced in powder conductivity measurements (shown in section 3.3.2). The uniform shell on the 3 $m^2\,g^{-1}$ TiO_2 support could directly result from the relatively thick nominal IrO_2 shells that form on the low surface area support (cf. calculated IrO_2 shell thicknesses in Table 2).

Physical characterization reveals that high IrO_2 contents and small

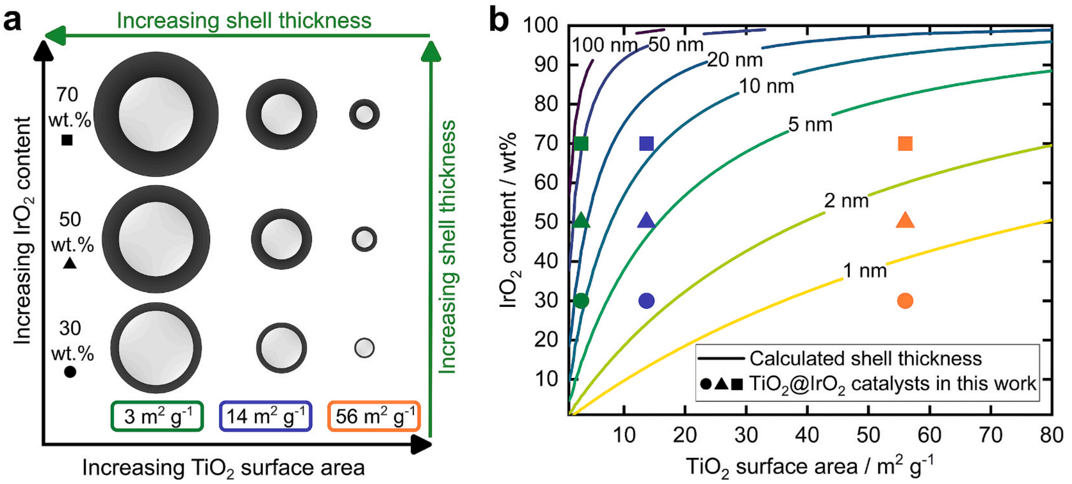

Fig. 1. (a) Schematic of $TiO_2@IrO_2$ particles showing the increased shell thickness for higher iridium contents and larger support particles (= smaller specific surface area). Square, triangle, and circle denote the different IrO_2 contents used throughout the study. (b) Contour plot of the calculated nominal IrO_2 shell thicknesses as a function of IrO_2 content and TiO_2 specific surface area. The calculation assumes a homogeneous and non-porous IrO_2 shell on spherical and monodisperse TiO_2 supports.

Table 2
Calculated nominal shell thicknesses (in nm) of the $TiO_2@IrO_2$ particles depending on the measured specific surface area of the TiO_2 support and the nominal IrO_2 content.

	3 m^2 g^{-1} TiO_2	14 m^2 g^{-1} TiO_2	56 m^2 g^{-1} TiO_2
70 wt% IrO_2	53.6	11.8	2.9
50 wt% IrO_2	25.7	5.7	1.4
30 wt% IrO_2	11.7	2.6	0.6

TiO_2 particles (i.e., large specific surface area) are not suitable for producing the desired core–shell structure with our synthesis method:

Using the 14 m^2 g^{-1} TiO_2 support, a relatively homogeneous particle shell is obtained for 50 wt% IrO_2 (Fig. 2c). Contrarily, for 70 wt% (Fig. 2d), we observe a non-continuous shell structure containing larger and seemingly denser IrO_2 clusters, accompanied by unsupported IrO_2 particles (Fig. S7) and a lower specific surface area (Fig. S10). This suggests that our synthesis method is not well suited for IrO_2 contents as high as 70 wt%. However, the exact formation pathway of the IrO_2 clusters remains to be investigated.

We do not observe a continuous shell structure for the 56 m^2 g^{-1} TiO_2 support with 50 wt% IrO_2 (Fig. 2e). Possibly, the specific surface area of the support is too large: As calculated, a shell thickness < 2 nm would be necessary to homogeneously cover this support at an iridium content of 50 wt% IrO_2 (cf. Table 2). Such a thin shell would require the individual iridium oxide crystallites to be smaller than 2 nm. However, Rietveld refinement of the XRD diffractogram (of 50 wt% IrO_2, 3 m^2 g^{-1} TiO_2; shown in Fig. 2f) reveals an average crystallite size of 7.3 ± 0.3 nm. For the catalyst with 50 wt% IrO_2 on the 56 m^2 g^{-1} TiO_2 support, a similar crystallite size can be estimated from the HAADF-STEM images in Fig. 2e, underlining that a continuous shell with a thickness of <2 nm is unfavored.

Furthermore, XRD pattern analysis (Fig. 2f) confirms the presence of rutile IrO_2, with no indication of metallic iridium. Additionally, we conducted high-resolution HAADF-STEM analyses (diffractograms in Fig. S11) on the other synthesized catalysts, which consistently show that the catalyst phase is rutile IrO_2 in all $TiO_2@IrO_2$ catalysts synthesized.

3.3. *Electrochemical characterization*

3.3.1. *OER mass activity*

All synthesized catalysts were tested in an RDE setup to analyze their catalytic activity for the oxygen evolution reaction. The resulting RDE curves are presented in Fig. 3a-c, alongside a commercially available IrO_2/TiO_2 catalyst from Umicore (88 wt% IrO_2, 75 wt% Ir) for comparison (denoted by the black line).

Evidently, the OER activities vary a lot between the synthesized samples, ranging from barely any activity (30 wt% IrO_2, 56 m^2 g^{-1} TiO_2) to an activity that exceeds the performance of the reference catalyst (e.g., 50 wt% IrO_2, 3 m^2 g^{-1} TiO_2).

The mass activity of all catalysts was assessed in the linear Tafel region (at 1.55 V vs. RHE, cf. Fig. S12) and plotted against the nominal shell thickness in Fig. 3d. The results show that catalysts with thicker shells generally have higher mass activities. To understand this trend, the pseudocapacitive responses and the corresponding capacitance-normalized OER activities of the catalysts were examined (Fig. 3e; detailed analysis in Fig. S13 and Table S2). This breakdown of OER activity contributions clearly shows that the difference in OER activities stems from differences in the capacitive response, i.e., from a different number of active sites. Accordingly, the activity per active site is nearly the same for all nine catalysts as expected for catalysts with the same active species.

This observation aligns with our physical characterization and substantiates our hypothesis that a thicker IrO_2 shell enhances catalyst utilization by exhibiting improved percolation and connectivity among catalyst particles. Importantly, this phenomenon makes a difference of two orders of magnitude in mass activity, emphasizing that the electrical percolation within electrocatalysts is essential.

As the research on iridium-based catalysts focuses on catalysts with a low iridium content, this finding motivates using low-surface-area supports. With these, the iridium (oxide) phase exhibits a thicker shell at a given iridium content, leading to better percolation and, thus, higher iridium mass activity. For future research, we note that the percolation of the iridium phase is expected to decrease in importance if more conductive support particles are used because the support will contribute to the electric conduction pathways.

Additionally, we observe the highest mass activity for the catalysts with 50 wt% IrO_2 within each TiO_2 support particle size. In comparison, the respective catalysts with 70 wt% IrO_2 exhibit decreased mass activities (Fig. 3d, the colored background serves as a guide to the eye). The performance decrease of the 70 wt% samples can be explained by the observed IrO_2 clusters in the HAADF-STEM/EDX spectrum images (Fig. 2d) along with a decrease in surface area (cf. capacitances in Fig. 3e and BET surface areas in Fig. S10). This trend likely indicates an optimum for the chosen synthesis method and is expected to behave

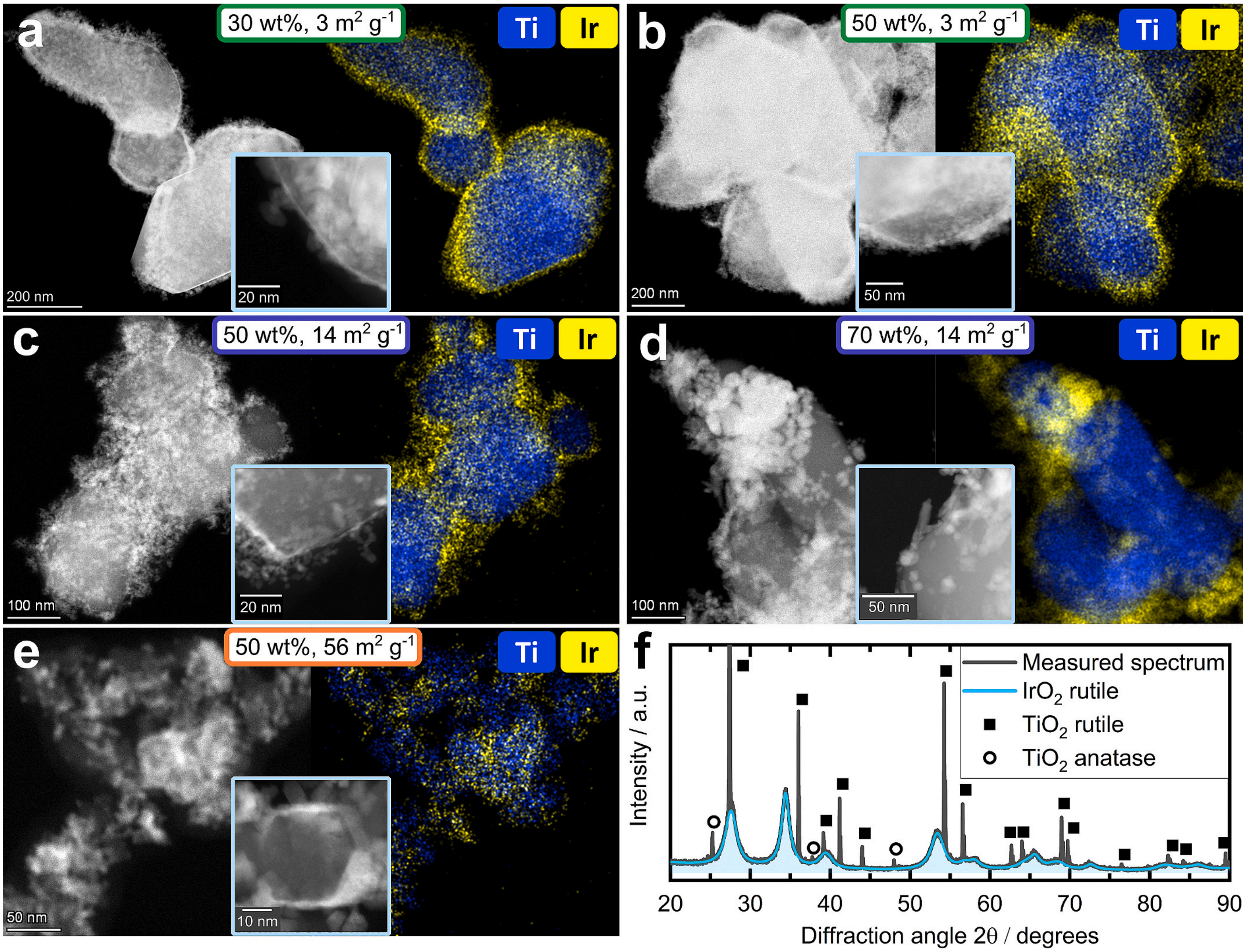

Fig. 2. (a-e) HAADF-STEM images and corresponding STEM-EDX spectrum images of five synthesized TiO_2@IrO_2 catalysts. The given wt% refers to the IrO_2 content, and the specific surface area refers to the TiO_2 particles. (f) XRD pattern of the TiO_2@IrO_2 catalyst with 50 wt% IrO_2 on 3 m^2 g^{-1} TiO_2 (shown in (b)). The IrO_2 contribution was fitted via Rietveld refinement.

differently for other synthesis approaches.

A slight increase in measurement uncertainty is noticeable for the three catalysts with 70 wt% IrO_2 (indicated by the shaded regions in Fig. 3c). This could potentially be attributed to the observed clustering of IrO_2 (see Fig. 2d), which might result in minor fluctuations due to the limited amount of catalyst present in the RDE measurement.

We expect no influence on the OER mechanism by changing the amount of iridium oxide in these catalysts as the active phase remains unchanged (rutile IrO_2, as shown in Fig. 2f and Fig. S11). This assessment is supported by similar Tafel slopes among all tested catalysts (Table S2), suggesting a consistent OER mechanism.

3.3.2. Powder conductivity

The conductivity of iridium-based catalysts is essential to ensure the electrical connection of the catalytic site and thus assist in fulfilling the triple-phase boundary condition of the CL. The powder conductivity measurements in Fig. 4a reveal significant differences between the catalysts, with conductivities spanning more than two orders of magnitude from <0.01 to 64 S cm^{-1}.

We observe an increase in conductivity with the IrO_2 content, which we relate to the higher volume fraction of the conductive iridium phase.

Interestingly, a higher conductivity is also obtained for support particles with lower surface areas. As all three different TiO_2 support particles exhibited a conductivity out of the measurable range of our setup ($< 10^{-2}$ S cm^{-1}), the direct participation of the TiO_2 in the conduction pathways can be excluded. However, by analyzing the powder conductivities depending on the nominal shell thickness (Fig. 4b), the formation of a thicker IrO_2 shell could again explain this effect. In general, we observe that a higher nominal shell thickness leads to an increased conductivity, even though this is not a strict trend: A higher IrO_2 content seems to have a more considerable influence on the conductivity than the particle size. We conclude this because the 70 wt% catalysts of a smaller support particle size exhibit a higher conductivity than the 30 wt% catalysts of a larger support particle size, even though the calculated shell thicknesses are similar (e.g., 70 wt% IrO_2, 14 m^2 g^{-1} TiO_2 shows a higher powder conductivity than 30 wt% IrO_2, 3 m^2 g^{-1} TiO_2).

Nonetheless, these trends further support the hypothesis that the nominal shell thickness can be used as a descriptor to optimize TiO_2@IrO_2 particles. Again, a strong argument must be made for support particles with a low specific surface area. Even employing a low IrO_2 content of only 30 wt%, the catalyst supported on the 3 m^2 g^{-1} TiO_2 particles exhibits a higher conductivity than nearly all other catalysts on support particles with a larger specific surface area. A lower iridium content in the catalyst powder enables the subsequent fabrication of low-loaded CLs while maintaining a sufficient layer thickness.

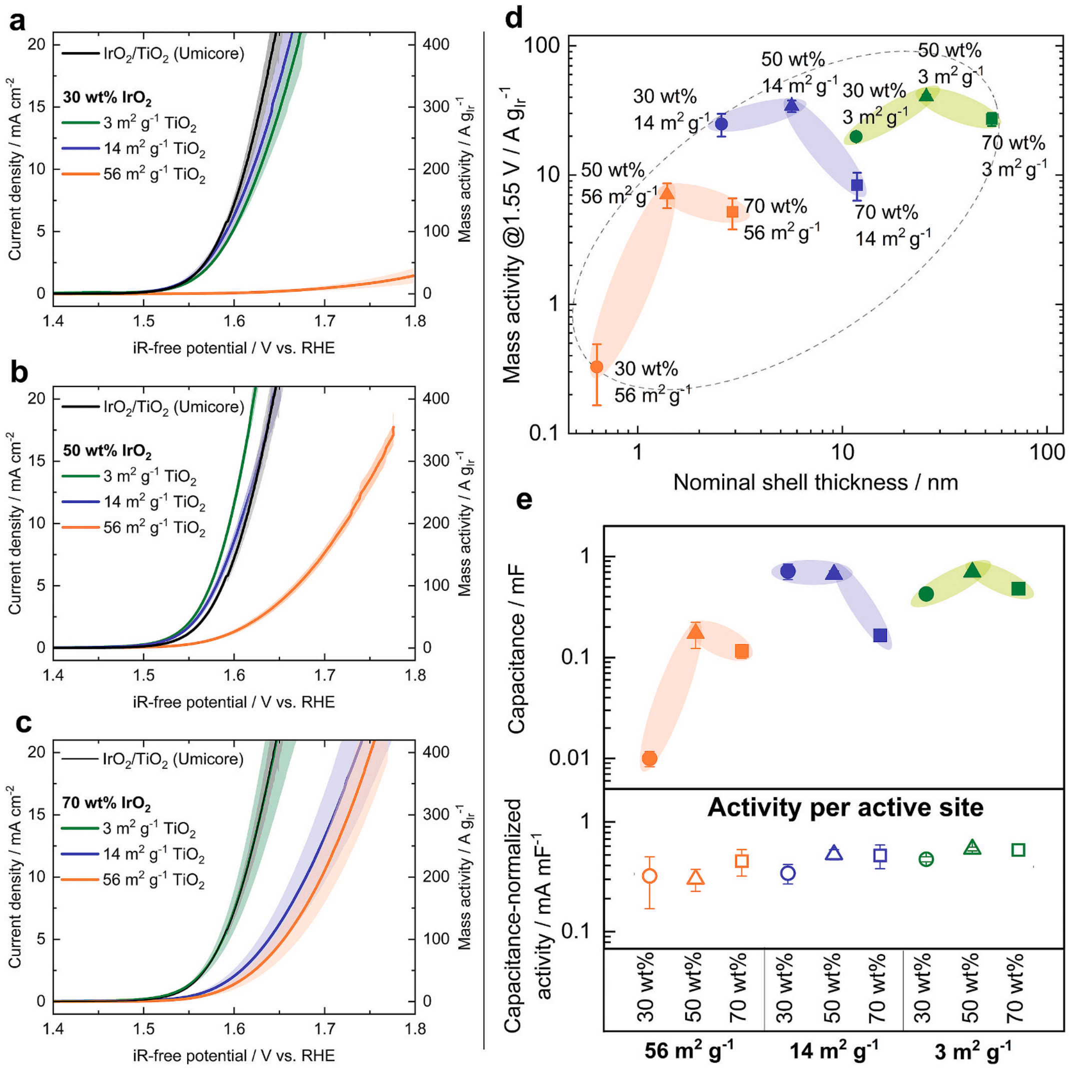

Fig. 3. OER activities of the nine different synthesized catalysts with (a) 30, (b) 50, and (c) 70 wt% IrO_2 on the different supports plus the reference catalyst IrO_2/TiO_2 (Umicore Elyst Ir75 0480). (d) Mass activities of the nine synthesized catalysts against the calculated IrO_2 shell thickness. (e) Capacitances and capacitance-normalized current densities (at 1.55 V vs. RHE) as a measure of the number of active sites and the activity per active site, respectively. The determination of the capacitances and the corresponding normalization are shown in detail in Fig. S13. Shaded areas in (a-c) and error bars in (d,e) depict the standard deviation of three separate measurements. The dotted ellipse and the colored background in (d,e) are a guide to the eye. All RDE measurements were conducted at a loading of 50 μg_{Ir} cm^{-2} in Ar-purged 0.1 M $HClO_4$.

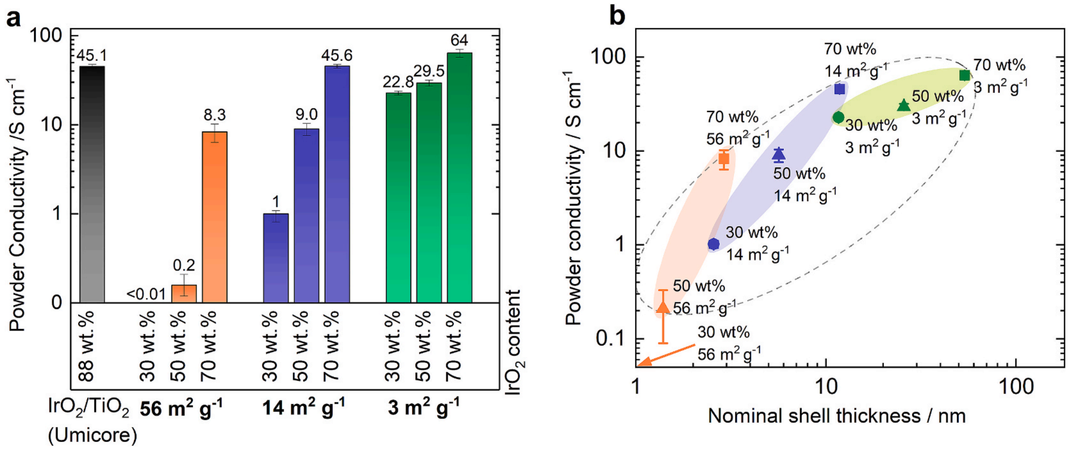

Fig. 4. (a) Powder conductivities of the nine TiO_2@IrO_2 catalysts and the commercial reference Umicore Elyst Ir75 0480. (b) The powder conductivities were plotted over the nominal IrO_2 shell thickness. Error bars depict the standard deviation of three separate measurements. The dotted ellipse and the colored background are a guide to the eye. The given wt% refers to the IrO_2 content, and the specific surface area refers to the TiO_2 particles.

Advancing this research direction, we show that large support particles can effectively enhance the conductivity of the catalyst when non-conductive supports are used.

We conclude that there is no distinct answer to our initial question of how much iridium is needed to form a percolating shell. Instead, relatively continuous trends are observed: Both mass activity and powder conductivity increase with an increasing nominal shell thickness. Within our chosen synthesis method, catalysts with an IrO_2 content of 50 wt% exhibit an optimal mass activity. Subsequently, this leads to the highest mass activity for the catalyst with 50 wt% IrO_2 on 3 $m^2\ g^{-1}$ TiO_2, as this represents the optimal IrO_2 content while at the same time forming the thickest possible shell due to the low surface area support.

3.3.3. *PEMWE single-cell testing*

Reducing the iridium content in the powder enables a subsequent reduction of the iridium loading in the CL while maintaining a sufficient layer thickness. Therefore, we test the novel catalysts toward this aim *via* 5 cm^2 PEMWE single-cell tests at low iridium loadings of 0.4 $mg_{Ir}\ cm^{-2}$ and 0.1 $mg_{Ir}\ cm^{-2}$.

For this purpose, the best three $TiO_2@IrO_2$ catalysts were selected for single-cell testing based on the pre-testing results. Specifically, 50 wt% IrO_2 on 3 $m^2\ g^{-1}$ TiO_2 was chosen as the catalyst with the highest mass activity (40.4 $A\ g_{Ir}^{-1}$ at 1.55 V vs. RHE) and a high powder conductivity (29.5 $S\ cm^{-1}$). In comparison, 50 wt% IrO_2 on 14 $m^2\ g^{-1}$ TiO_2 was employed due to its similarly high mass activity (34.2 $A\ g_{Ir}^{-1}$) but a lower conductivity (9.0 $S\ cm^{-1}$). Lastly, 30 wt% IrO_2 on 3 $m^2\ g^{-1}$ TiO_2 was selected as a catalyst exhibiting a moderate mass activity (19.8 $A\ g_{Ir}^{-1}$) but a high conductivity (22.8 $S\ cm^{-1}$). We note that, although the catalyst with 70 wt% IrO_2 on 3 $m^2\ g^{-1}$ TiO_2 also showed high mass activity (27.1 $A\ g_{Ir}^{-1}$) and conductivity (64 $S\ cm^{-1}$) in pre-testing, it is not included in single-cell testing because the focus of this study lies on reducing the iridium content.

These three selected $TiO_2@IrO_2$ catalysts and the commercial IrO_2/TiO_2 reference catalyst were used to fabricate half-catalyst coated membranes (hCCMs) for testing in a single-cell PEMWE setup. The resulting polarization curves and the fitted high frequency resistances (HFRs) are shown in Fig. 5.

Fig. 5a shows that the catalyst with 50 wt%, 14 $m^2\ g^{-1}$ has the lowest performance of all single-cell tests with 0.4 $mg_{Ir}\ cm^{-2}$. This can be attributed to a particularly high HFR, which correlates with its low powder conductivity (9.0 $S\ cm^{-1}$, cf. Fig. 4). Also, this catalyst shows a steeper increase in HFR–free potential than the other $TiO_2@IrO_2$ catalysts. This effect possibly indicates a lower catalyst utilization, which a low catalyst conductivity could cause [31]. We note that this significant influence of the low catalyst conductivity on the HFR should be prevented by coating the titanium PTLs with platinum or iridium, as shown in the literature [21,32,33]. However, whether these coatings can also prevent a decreased catalyst utilization is unclear.

The 30 wt%, 3 $m^2\ g^{-1}$ sample performs worse than the reference and the 50 wt%, 3 $m^2\ g^{-1}$ catalyst, which can be traced back to a slightly increased HFR and a higher HFR-free potential. The increased HFR could possibly be attributed to the thickest CL, which is expected because of the lowest IrO_2 content of this catalyst. The higher HFR-free potential aligns with the mass activity measurements in RDE, which showed the lowest mass activity for the 30 wt%, 3 $m^2\ g^{-1}$ catalyst within the three $TiO_2@IrO_2$ catalysts tested in a single cell. The exact reason for the lower activity is unknown. A possible explanation could relate to the thinner shell thickness of the IrO_2 phase or the chosen synthesis method that shows an optimal mass activity for an iridium oxide content of 50 wt%, as discussed before.

At a loading of 0.4 $mg_{Ir}\ cm^{-2}$, the $TiO_2@IrO_2$ catalyst with 50 wt%, 3 $m^2\ g^{-1}$ performs equally well as the IrO_2/TiO_2 reference catalyst. Both exhibit similar HFR values and HFR-free potentials. Analyzing the HFR-free potentials reveals a lower *apparent* Tafel slope for the $TiO_2@IrO_2$ catalyst (47.0 ± 0.1 mV dec^{-1}; Fig. S14a) than for the reference (52.3 ± 0.7 mV dec^{-1}). This difference does not stem from different iridium phases, as our synthesis method yields a rutile iridium oxide (cf. Fig. 2f), which is the same as the active phase of the reference catalyst [9].

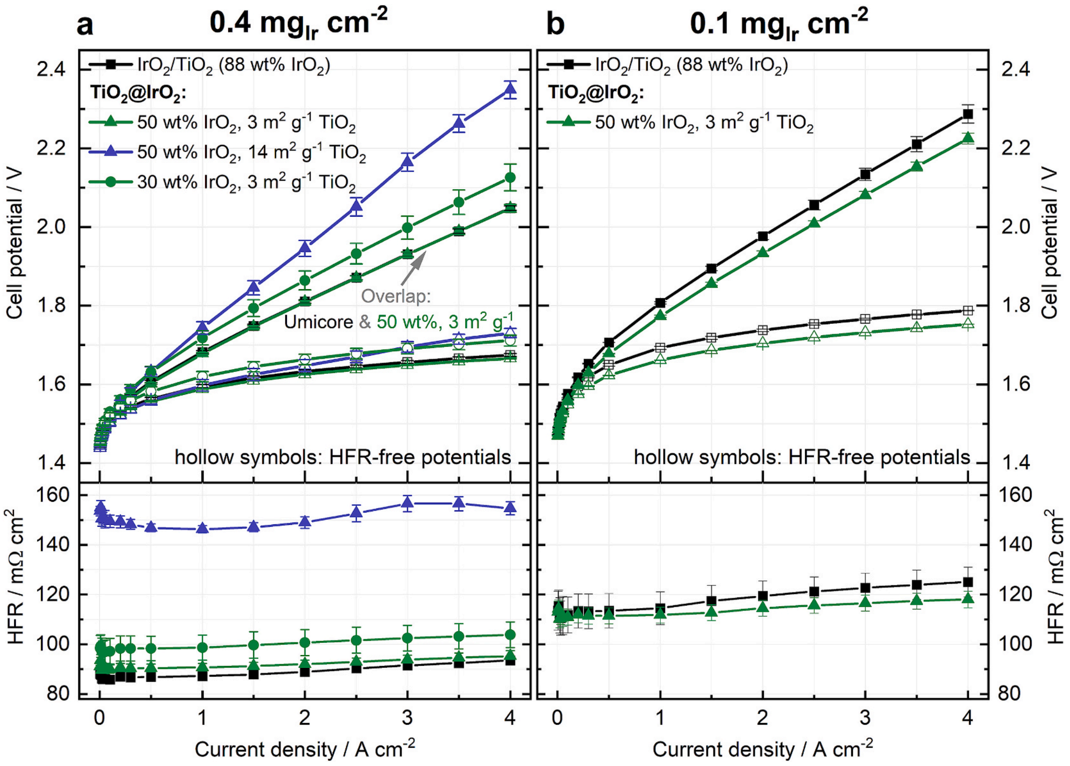

Fig. 5. Polarization curves and HFR values of 5 cm^2 PEMWE single-cell tests at iridium loadings of (a) 0.40 ± 0.01 and (b) 0.10 ± 0.01 $mg_{Ir}\ cm^{-2}$. Error bars depict the min–max deviation of two separate single-cell measurements. All cell tests were performed at 80 °C, ambient pressure, and an H_2O flow rate of 100 mL min^{-1}. An uncoated Ti-fiber PTL and an hCCM (on Nafion NR212) were used on the anode side, and a commercial GDE (0.5 $mg_{Pt}\ cm^{-2}$ on carbon cloth) on the cathode side.

Instead, at higher loadings (> 1 $mg_{Ir}\ cm^{-2}$), a Tafel slope of 45–50 mV dec^{-1} is usually also observed for the reference catalyst, as shown elsewhere [6,28]. This slope generally increases when the CL gets too thin because additional contributions are reflected in the *apparent* Tafel slope [6,28]. The slightly increased *apparent* Tafel slope for the reference catalyst is thus an indicator for utilization losses, which aligns with the reported threshold loading of ~0.5 $mg_{Ir}\ cm^{-2}$ for the reference catalyst, below which the CL gets too thin and becomes non-contiguous [6]. Unlike the commercial reference, all three TiO_2@IrO_2 catalysts exhibit Tafel slopes in the expected range of 45–50 mV dec^{-1}. These values indicate that the CL exhibits sufficient thickness and the layer structure stays intact. The decreased iridium content in these catalysts can explain the sufficient CL thickness, resulting in a thicker CL at a given loading.

Decreasing the loading to 0.1 $mg_{Ir}\ cm^{-2}$ further amplifies the effects observed for non-contiguous CLs (Fig. 5b): Now, the TiO_2@IrO_2 catalyst (50 wt%, 3 $m^2\ g^{-1}$) outperforms the commercial reference catalyst by 43 mV at 2 A cm^{-2} and 63 mV at 4 A cm^{-2}. A breakdown of the voltage losses reveals that the difference mainly stems from HFR-free potential contributions, i.e., from the CL activity. Again, we attribute this relative improvement of the TiO_2@IrO_2 catalyst performance to the thicker CL, maintaining a more intact structure at this low loading. This explanation is further supported by the trends in the apparent Tafel slopes (Fig. S14b). At 0.1 $mg_{Ir}\ cm^{-2}$, the apparent Tafel slope of the reference catalyst increases to 65.7 ± 0.5 mV dec^{-1} (increase by 13.4 mV dec^{-1}), suggesting a further decreased connectivity within the CL. This increase in the apparent Tafel slope for the Umicore IrO_2/TiO_2 catalyst aligns with previous reports [6]. The apparent Tafel slope of the TiO_2@IrO_2 catalyst also increases, but to a lesser extent, by 9.2 mV dec^{-1} to 56.2 ± 0.5 mV dec^{-1}. We interpret this as the same effect of CL non-contiguousness, which also onsets for the TiO_2@IrO_2 catalyst at this low loading but is less pronounced. The relationship between the iridium content, the CL thickness, and the according disconnection at this low loading is schematically shown in Fig. 6.

Comparing the single-cells with 0.1 $mg_{Ir}\ cm^{-2}$ to 0.4 $mg_{Ir}\ cm^{-2}$ shows an increased HFR of ca. 25 mΩ cm^2, as well as an increase in HFR-free potential of 43 and 71 mV at 0.1 A cm^{-2} for the TiO_2@IrO_2 and the reference catalyst, respectively. The increase in HFR-free potential is higher than expected from purely OER kinetics (expected increase of 27–30 mV from the respective Tafel slopes). This further proves that, for both catalysts, the utilization of the CL decreases when decreasing the loading to 0.1 $mg_{Ir}\ cm^{-2}$. Once more, this effect is less pronounced for the TiO_2@IrO_2 catalyst than for the reference catalyst, indicating that a higher degree of connection within the CL is maintained.

All the discussed electrochemical indicators clearly show that the reference CL suffers from severe disconnection, as schematically shown in Fig. 6. We attribute this to the extremely thin CL at 0.1 $mg_{Ir}\ cm^{-2}$, with an estimated thickness of only 0.4 μm, according to previously determined thickness factors of approximately 4 μm $(mg_{Ir}\ cm^{-2})^{-1}$ [6,12]. While the TiO_2@IrO_2 catalyst (50 wt% IrO_2, 3 $m^2\ g^{-1}$ TiO_2) did not show significant signs of CL disconnection at 0.4 $mg_{Ir}\ cm^{-2}$, a performance decrease due to disconnection can be observed at 0.1 $mg_{Ir}\ cm^{-2}$. Consequently, to fabricate sufficiently thick CLs at a low loading of 0.1 $mg_{Ir}\ cm^{-2}$, the iridium content in the powder needs to be further decreased, as schematically shown in Fig. 6. Therefore, a continued aim of future research should be developing catalyst synthesis methods that enable a low iridium content while maintaining a high mass activity and employing stable materials.

We note that decreasing the iridium content in the catalyst is not the only way of maintaining a continuous CL at low iridium loadings – alternative approaches such as employing 1D (nanowires, nanofibers, et cetera) [34–38] or 2D catalyst geometries (nanosheets) [39,40], fabricating highly porous CLs [41,42] or employing microporous transport layers (MPLs) onto the PTLs [43–45] are also promising approaches. The MPL approach is especially interesting in this context as it can possibly attenuate the localized forces on the CL, leaving more room for optimization from the CL side.

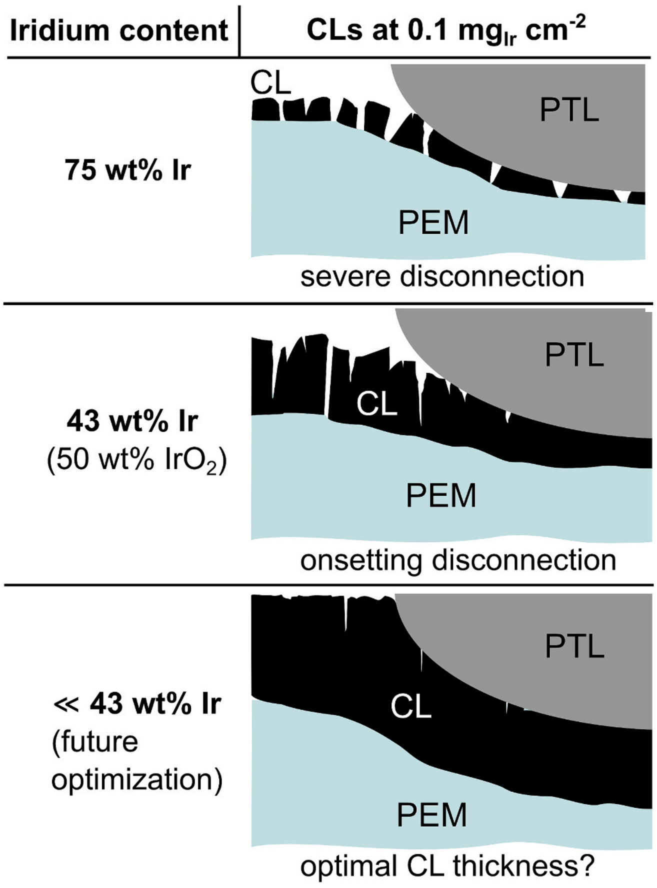

Fig. 6. Schematic demonstrating the CL thickness and the resulting disconnection within the CL for catalysts with different iridium contents at a low CL loading of 0.1 $mg_{Ir}\ cm^{-2}$.

We speculate that an intact CL likely maintains not only a high activity but also a higher long-term stability, as it has been shown that the formation of hot spots can decrease the stability of non-contiguous CLs [46–48]. To get an impression of the stability of the synthesized catalysts in this study, PEMWE stability testing of one TiO_2@IrO_2 catalyst was performed. More precisely, the best-performing TiO_2@IrO_2 catalyst (50 wt% IrO_2 on 3 $m^2\ g^{-1}$ TiO_2) and the reference catalyst were tested at a loading of 0.4 $mg_{Ir}\ cm^{-2}$ for 200 h at 2 A cm^{-2}. The recorded potential evolution and polarization curves are shown in Fig. S15. The TiO_2@IrO_2 catalyst exhibits a higher degradation rate in the first 100 h and stabilizes afterward. In the last 30 h of testing, the cell shows a promisingly low degradation rate of 0.07 mV h^{-1}, which is in the lower range of recent literature results in which degradation rates between 0.006 and 0.57 mV h^{-1} are reported (cf. Table S3 for literature comparison). This low degradation rate is encouraging, especially when compared to our previous study [9], in which the TiO_2@IrO_2 catalyst showed lower dissolution stability in half-cell measurements. The single-cell testing presented here reveals that the catalyst degradation can stabilize within the first few hundred hours, nonetheless, as also shown in literature [20,49]. While longer stability tests are needed to confirm the catalyst's commercial viability, our initial results are promising. Furthermore, end-of-test HAADF-STEM analysis of the catalyst reveals no significant structural changes, as shown in Fig. S16.

Overall, the single-cell results indicate that catalyst conductivity and mass activity are essential parameters for an optimized PEMWE performance. The TiO_2@IrO_2 catalyst with 50 wt% IrO_2 on 3 $m^2\ g^{-1}$ TiO_2 support shows an optimal performance within the chosen synthesis method and parameters. Importantly, this catalyst exhibits a smaller performance decrease than the commercial reference catalyst when the iridium loading is reduced to 0.1 $mg_{Ir}\ cm^{-2}$, thereby outperforming the reference catalyst. We attribute this relative improvement to the decreased iridium content of the $TiO_2@IrO_2$ catalyst, resulting in a thicker CL and thereby preventing crack formation and disconnection. Consequently, a higher iridium-specific power density at 1.79 V (i.e., at 70 % efficiency of the lower heating value) [6] can be reached. At 0.1 $mg_{Ir}\ cm^{-2}$, the $TiO_2@IrO_2$ catalyst exhibits a 20 % higher power density (19.8 $kW\ g_{Ir}^{-1}$) than the reference catalyst (16.4 $kW\ g_{Ir}^{-1}$), emphasizing the benefits of low-iridium catalysts in improving iridium utilization (cf. Table S3 for literature comparison [50–52]).

As the trends observed in pre-testing are fairly pronounced, we now clarify how well these *ex situ* results relate to the single-cell results. In other words, how accurately can our catalyst pre-testing predict the performance of an electrolyzer?

3.4. Comparison ex situ testing vs. Single-cell testing

The advantage of e*x situ* testing over single-cell testing is the ability to screen many catalysts in a comparably short time. However, e*x situ* testing can only be meaningful if it reflects the same trends as single-cell testing. As this study produced catalysts with a broad variation of conductivities and mass activities, it is further used to investigate how well the employed pre-testing methods, RDE and powder conductivity, correlate with the performance of a single-cell electrolyzer using the respective catalyst.

3.4.1. RDE mass activity vs. Single-cell mass activity

First, the ohmic-resistance-corrected mass activities are compared. As RDE and single-cell testing are performed at different operating temperatures, the mass activities are determined at different potentials. The potentials are chosen to lie within the linear Tafel region of the respective measurements, as exemplified in Fig. S12. In Fig. 7a and b, the determined mass activities are plotted as bar graph and correlation plot, respectively.

Although the data points have relatively high uncertainties, a general trend of higher mass activity in RDE is reflected in a higher mass activity in the single cell. This correlation is confirmed by a moderately high Pearson correlation coefficient (Pearson R) of 0.76. Generally, a Pearson R between 0.7 and 1.0 is considered a strong positive correlation [53]. We emphasize that only four data points are analyzed, and more research should focus on this correlation. Additionally, the large 95 % confidence interval in Fig. 7b emphasizes that the yielded accuracy is only providing a first estimate. Possible reasons for deviation could stem from either measurement technique, RDE, or single-cell testing.

Studies have demonstrated that bubble formation can impact mass activity results in RDE by obstructing active surface sites [54,55]. In single-cell testing, the extent of catalyst utilization within the CL has a significant effect on mass activity [6,31,45,56]. Catalyst utilization, in turn, is influenced by the conductivity of the CL, which can be compromised by crack formation [31,37]. Furthermore, other factors that may affect mass activity in single-cell measurements include the interface between the PTL and CL (factors such as contact area, pore size, and CL deformation) [6,31,45,57–59], as well as the possible impact of ionomer distribution within the CL [60,61], which is necessary for meeting the triple-phase boundary condition. These effects may potentially contribute to the observed variability in mass activity during single-cell testing (error bars in Fig. 7a and b). However, it is worth noting that this variability appears to have a diminishing impact on the performance at higher current densities, as evidenced by the generally good reproducibility of the polarization curves in Fig. 5.

Because of all these different influences in both measurement techniques, we conclude that RDE can be used to evaluate trends, especially by comparing different catalysts under the same measurement conditions. However, it might be difficult to compare the absolute mass activities between different laboratories – here, we emphasize the importance of measuring reference samples. Furthermore, minor differences in RDE results should not be over-interpreted. Instead, RDE should be used to ensure that a catalyst activity is sufficiently high, and single-cell testing should follow early in catalyst development studies to determine the actual performance of a catalyst. Especially at low iridium loadings, the single-cell performance can be influenced by additional parameters during single-cell testing, such as catalyst conductivity. This conclusion aligns with previous studies comparing RDE and single-cell mass activities [55,62].

3.4.2. Powder resistivity vs. Single-cell HFR

Next, the resistivities of the catalysts from powder conductivity measurement and single-cell testing are compared. Therefore, the powder conductivities are expressed as powder resistivities and compared to the average HFRs from single-cell testing. Again, the comparison of the two measurement techniques is shown as a bar graph and correlation plot in Fig. 8a and b.

Remarkably, a strong correlation with a Pearson R of 0.99 is observed. As shown in Fig. 8b, a high powder resistivity (i.e., low powder conductivity) is clearly reflected in an increased HFR in the single-cell measurements. To further validate this correlation, the in-plane resistances of the coated catalyst layers were determined. As shown in Fig. S17a, an identical correlation between in-plane resistance and HFR is observed (Pearson R: 0.99), showcasing the comparability of the three different resistance measurements (Fig. S17b). Again, we

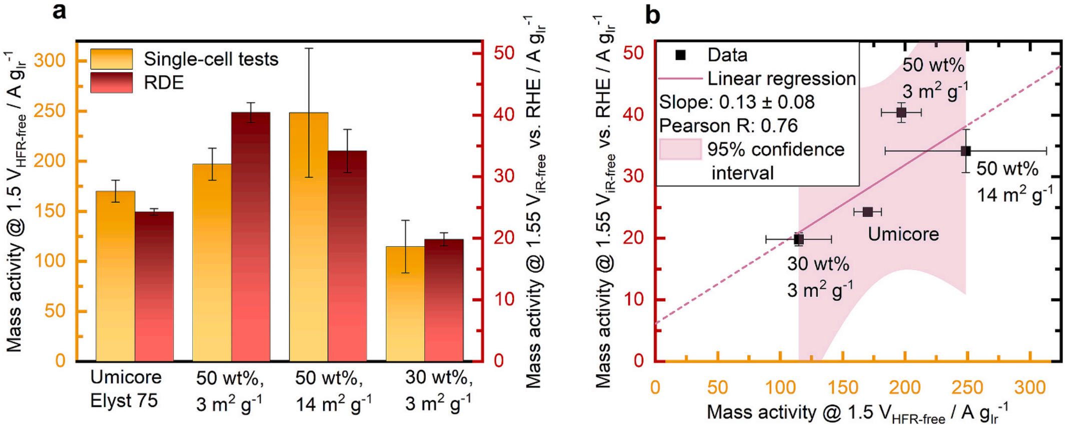

Fig. 7. Comparison of the resistance-corrected mass activities in pre-testing (RDE) and single-cell testing as (a) bar graph and (b) correlation plot. Error bars of the RDE results depict the standard deviation of three separate measurements. Error bars of the single-cell results depict the min–max deviation of two separate measurements. The given wt% refers to the IrO_2 content, and the specific surface area refers to the TiO_2 particles. A Deming regression (accounting for x and y error) is used as a linear regression model to evaluate the degree of correlation, which is expressed in the correlation coefficient Pearson R.

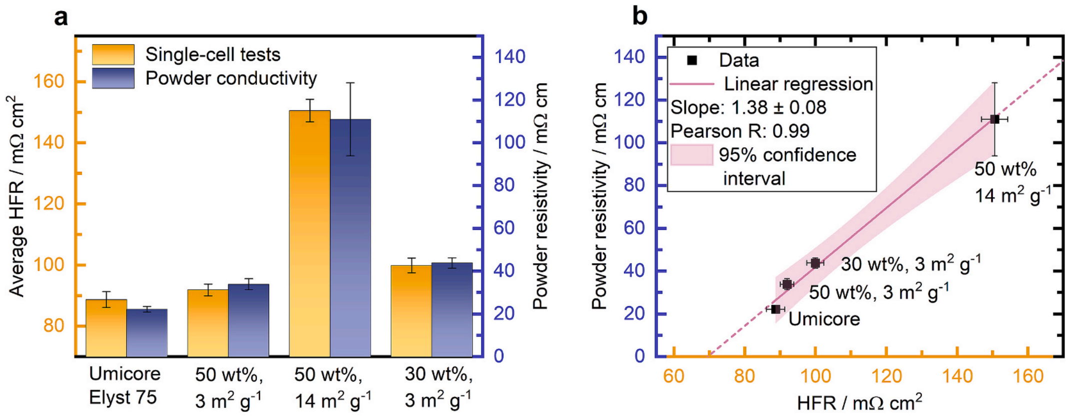

Fig. 8. Comparison of the resistivities in pre-testing (powder resistivity) and single-cell testing (HFR) as (a) bar graph and (b) correlation plot. Error bars of the powder resistivities depict the standard deviation of three separate measurements. HFR values were averaged between 0.5 and 4 A cm^{-2}. Error bars of the HFR from single-cell testing depict the min–max deviation of two separate measurements at a loading of 0.4 mg$_{Ir}$ cm^{-2}. The given wt% refers to the IrO_2 content, and the specific surface area refers to the TiO_2 particles. A Deming regression (accounting for x and y error) is used as a linear regression model to evaluate the degree of correlation, which is expressed in the correlation coefficient Pearson R.

emphasize that the single-cell HFRs might behave differently for noble-metal-coated PTLs. However, when using uncoated PTLs, as done in this study, the powder resistivity is highly important and should be minimized, i.e., the powder conductivity of the catalyst should be maximized.

The *x*-intercept of the correlation plot in Fig. 8b is approximately 70 mΩ cm^2. As this corresponds to zero resistance from the catalyst powder, this value should reflect the sum of all other resistances in the electrolyzer cell. Assuming a typical membrane conductivity between 0.11 and 0.19 S cm^{-1} for Nafion membranes [63,64], and a wet thickness of ~64 μm [65], a protonic resistance between 34 and 58 mΩ cm^2 can be estimated for a Nafion NR212 membrane. This leaves between 12 and 36 mΩ cm^2 for the additional bulk and interface resistances in the cell. This estimation emphasizes the importance of the catalyst conductivity, whose contribution to the cell resistance (between 19 and 80 mΩ cm^2) is on the same order of magnitude as all other bulk and interface resistances (apart from the membrane resistance).

4. Conclusion

Using a previously developed synthesis route, nine different TiO_2 supported IrO_2 catalysts with an IrO_2 particle shell (TiO_2@IrO_2) with three different IrO_2 contents (30, 50, and 70 wt%) on three different TiO_2 supports (3, 14, and 56 m^2 g^{-1}) were synthesized and systematically analyzed.

Relating the measured performances to a calculated nominal IrO_2 shell thickness for these catalysts reveals intriguing trends: Both higher mass activities and higher conductivities are obtained for TiO_2@IrO_2 particles with a thicker nominal IrO_2 shell, indicating that the nominal IrO_2 shell thickness can be used as an adequate descriptor to optimize these catalysts. Various research currently focuses on decreasing the iridium content in the catalyst powder. In this context, a strong argument is made in favor of support particles with a low specific surface area (i.e., large support particles), as they allow the formation of a relatively thick IrO_2 shell.

Testing the best three synthesized TiO_2@IrO_2 catalysts in a PEMWE single-cell setup reveals that the trends of the employed pre-testing methods, RDE, and powder conductivity can generally be observed in single-cell testing. The ohmic-resistance free mass activities correlate moderately, whereas a strong correlation is observed for the resistivities.

Accordingly, the TiO_2@IrO_2 catalyst that exhibited the highest mass activity and one of the highest powder conductivities during pre-testing, namely 50 wt% IrO_2 on 3 m^2 g^{-1} TiO_2 support, is also the best-performing catalyst in the single-cell electrolyzer. At a loading of 0.4 mg$_{Ir}$ cm^{-2}, its performance is on par with that of the commercial reference catalyst. When the loading is further reduced to 0.1 mg$_{Ir}$ cm^{-2}, this TiO_2@IrO_2 catalyst outperforms the reference catalyst by 43 mV at 2 A cm^{-2}. This relative improvement is ascribed to the lower iridium content in the TiO_2@IrO_2 catalyst, resulting in a thicker CL. These findings further emphasize that the anodic CL in PEMWE needs to be sufficiently thick, which, for low iridium loadings, can be achieved by reducing the iridium content in the catalyst powder.

While in our previous work, the TiO_2@IrO_2 catalyst with 50 wt% IrO_2 on 3 m^2 g^{-1} TiO_2 outperformed the commercial reference catalyst in a porous transport electrode (PTE) configuration at higher iridium loadings (0.4 and 1.2 mg$_{Ir}$ cm^{-2}), in this work an improved performance of the TiO_2@IrO_2 catalyst was only observed at 0.1 mg$_{Ir}$ cm^{-2} in an hCCM configuration. This is ascribed to a severe crack formation in the reference CL. This discrepancy between the PTE and hCCM results raises the research question of whether the effects stemming from a non-contiguous CL could also explain the differences observed in the PTE configuration.

Future research should focus on developing TiO_2@IrO_2 synthesis methods that further decrease the iridium content without compromising electrochemical activity. Additionally, the stability of catalysts with low iridium content should be investigated systematically as degradation mechanisms of catalyst layers with low loadings could substantially differ from those of catalyst layers with high loadings. Furthermore, research efforts to find alternative support materials with higher conductivity than TiO_2 should continue. Given the scarcity of iridium, it is also essential to continue exploring alternative catalyst materials, particularly those based on non–noble metals such as manganese oxides [66,67] or cobalt oxides [68,69].

Data and Code availability

The raw data and the Rietveld refinement of the reported XRD diffractogram in Fig. 2f are available at Zenodo under the following https://doi.org/10.5281/zenodo.13944306.

The Python routine for the averaging of polarization curve data and HFR fitting of the electrochemical impedance spectroscopy measurements is available on Zenodo under the following https://doi.org/10.5281/zenodo.13969896 [70].

CRediT authorship contribution statement

Darius Hoffmeister: Writing – review & editing, Writing – original draft, Visualization, Validation, Methodology, Investigation, Formal analysis, Conceptualization. **Selina Finger:** Writing – review & editing, Validation, Software, Investigation. **Ramesh Pokhrel:** Writing – review & editing, Validation, Investigation, Formal analysis, Conceptualization. **Andreas Körner:** Writing – review & editing, Investigation. **Birk Fritsch:** Writing – review & editing, Supervision, Software, Methodology, Investigation. **Simon Thiele:** Writing – review & editing, Supervision, Resources, Project administration, Funding acquisition. **Andreas Hutzler:** Writing – review & editing, Supervision, Project administration, Investigation, Funding acquisition, Conceptualization. **Chuyen van Pham:** Writing – review & editing, Supervision, Project administration, Funding acquisition, Conceptualization.

Declaration of competing interest

Acknowledgements

The authors gratefully acknowledge the financial support by the German Federal Ministry of Education and Research (BMBF) for the project StacIE (FKZ: 03HY103H) within the H_2Giga flagship project. Furthermore, the authors thank Andreas Göpfert for the XRD measurement and Theresa Stigler and Dennis Chalupczok for TGA measurements.

Appendix A. Supplementary data

Supplementary data to this article can be found online at https://doi.org/10.1016/j.cej.2025.164281.

References

[1] C. Minke, M. Suermann, B. Bensmann, R. Hanke-Rauschenbach, Is iridium demand a potential bottleneck in the realization of large-scale PEM water electrolysis? Int. J. Hydrog. Energy 46 (2021) 23581–23590, https://doi.org/10.1016/j.ijhydene.2021.04.174.

[2] C. van Pham, D. Escalera-López, K. Mayrhofer, S. Cherevko, S. Thiele, Essentials of high performance water electrolyzers – From catalyst layer materials to electrode engineering, Adv. Energy Mater. (2021) 2101998, https://doi.org/10.1002/aenm.202101998.

[3] Y. Xu, Y. Zhao, Z. Yuan, Y. Sun, S. Peng, Y. Zhong, M. Sun, L. Yu, Balancing the relationship between the activity and stability of anode oxide-based electrocatalysts in acid for PEMWE electrolyzers, J. Mater. Chem. A 12 (2024) 18751–18773, https://doi.org/10.1039/D4TA02869D.

[4] J. Knöppel, M. Möckl, D. Escalera-López, K. Stojanovski, M. Bierling, T. Böhm, S. Thiele, M. Rzepka, S. Cherevko, On the limitations in assessing stability of oxygen evolution catalysts using aqueous model electrochemical cells, Nat. Commun. 12 (2021) 2231, https://doi.org/10.1038/s41467-021-22296-9.

[5] S. Cherevko, Stability and dissolution of electrocatalysts: Building the bridge between model and "real world" systems, Curr. Opin. Electrochem. 8 (2018) 118–125, https://doi.org/10.1016/j.coelec.2018.03.034.

[6] M. Bernt, A. Siebel, H.A. Gasteiger, Analysis of voltage losses in PEM water electrolyzers with low platinum group metal loadings, J. Electrochem. Soc. 165 (2018) F305–F314, https://doi.org/10.1149/2.0641805jes.

[7] U. Babic, M. Suermann, F.N. Büchi, L. Gubler, T.J. Schmidt, Critical review—identifying critical gaps for polymer electrolyte water electrolysis development, J. Electrochem. Soc. 164 (2017) F387–F399, https://doi.org/10.1149/2.1441704jes.

[8] M. Clapp, C.M. Zalitis, M. Ryan, Perspectives on current and future iridium demand and iridium oxide catalysts for PEM water electrolysis, Catal. Today 420 (2023) 114140, https://doi.org/10.1016/j.cattod.2023.114140.

[9] C. van Pham, M. Bühler, J. Knöppel, M. Bierling, D. Seeberger, D. Escalera-López, K.J. Mayrhofer, S. Cherevko, S. Thiele, IrO2 coated TiO2 core-shell microparticles advance performance of low loading proton exchange membrane water electrolyzers, Appl. Catal. B 269 (2020) 118762, https://doi.org/10.1016/j.apcatb.2020.118762.

[10] M. Mandal, M. Secanell, Improved polymer electrolyte membrane water electrolyzer performance by using carbon black as a pore former in the anode catalyst layer, J. Power Sources 541 (2022) 231629, https://doi.org/10.1016/j.jpowsour.2022.231629.

[11] J. Kwen, G. Doo, S. Choi, H. Guim, S. Yuk, D.-H. Lee, D.W. Lee, J. Hyun, H.-T. Kim, Identification of the electrical connection in the catalyst layer of the polymer electrolyte membrane water electrolyzer, Int. J. Hydrog. Energy 47 (2022) 14017–14026, https://doi.org/10.1016/j.ijhydene.2022.02.136.

[12] D. Hoffmeister, S. Finger, L. Fiedler, T.-C. Ma, A. Körner, M. Zlatar, B. Fritsch, K. W. Bodnar, S. Carl, A. Götz, B.A. Zubiri, J. Will, E. Spiecker, S. Cherevko, A.T. S. Freiberg, K.J.J. Mayrhofer, S. Thiele, A. Hutzler, C. van Pham, Photodeposition-based synthesis of TiO2@IrOx core-shell catalyst for proton exchange membrane water electrolysis with low iridium loading, Adv. Sci. 11 (2024) e2402991, https://doi.org/10.1002/advs.202402991.

[13] H. Lv, G. Zhang, C. Hao, C. Mi, W. Zhou, D. Yang, B. Li, C. Zhang, Activity of IrO 2 supported on tantalum-doped TiO 2 electrocatalyst for solid polymer electrolyte water electrolyzer, RSC Adv. 7 (2017) 40427–40436, https://doi.org/10.1039/C7RA06534E.

[14] D. Böhm, M. Beetz, M. Schuster, K. Peters, A.G. Hufnagel, M. Döblinger, B. Böller, T. Bein, D. Fattakhova-Rohlfing, Efficient OER catalyst with low ir volume density obtained by homogeneous deposition of iridium oxide nanoparticles on macroporous antimony-doped tin oxide support, Adv. Funct. Mater. 30 (2020) 1906670, https://doi.org/10.1002/adfm.201906670.

[15] A. Hartig-Weiss, M. Miller, H. Beyer, A. Schmitt, A. Siebel, A.T.S. Freiberg, H. A. Gasteiger, H.A. El-Sayed, Iridium oxide catalyst supported on antimony-doped tin oxide for high oxygen evolution reaction activity in acidic media, ACS Appl. Nano Mater. 3 (2020) 2185–2196, https://doi.org/10.1021/acsanm.9b02230.

[16] S.-B. Han, Y.-H. Mo, Y.-S. Lee, S.-G. Lee, D.-H. Park, K.-W. Park, Mesoporous iridium oxide/Sb-doped SnO2 nanostructured electrodes for polymer electrolyte membrane water electrolysis, Int. J. Hydrog. Energy 45 (2020) 1409–1416, https://doi.org/10.1016/j.ijhydene.2019.11.109.

[17] G.C. Da Silva, S.I. Venturini, S. Zhang, M. Löffler, C. Scheu, K.J.J. Mayrhofer, E. A. Ticianelli, S. Cherevko, Oxygen evolution reaction on tin oxides supported iridium catalysts: do we need dopants? ChemElectroChem 7 (2020) 2330–2339, https://doi.org/10.1002/celc.202000391.

[18] E. Oakton, D. Lebedev, M. Povia, D.F. Abbott, E. Fabbri, A. Fedorov, M. Nachtegaal, C. Copéret, T.J. Schmidt, IrO 2 -TiO 2 A high-surface-area active, and stable electrocatalyst for the oxygen evolution reaction, ACS Catal. 7 (2017) 2346–2352, https://doi.org/10.1021/acscatal.6b03246.

[19] D. Böhm, M. Beetz, C. Gebauer, M. Bernt, J. Schröter, M. Kornherr, F. Zoller, T. Bein, D. Fattakhova-Rohlfing, Highly conductive titania supported iridium oxide nanoparticles with low overall iridium density as OER catalyst for large-scale PEM electrolysis, Appl. Mater. Today 24 (2021) 101134, https://doi.org/10.1016/j.apmt.2021.101134.

[20] M. Möckl, M.F. Ernst, M. Kornherr, F. Allebrod, M. Bernt, J. Byrknes, C. Eickes, C. Gebauer, A. Moskovtseva, H.A. Gasteiger, Durability testing of low-iridium PEM water electrolysis membrane electrode assemblies, J. Electrochem. Soc. 169 (2022) 64505, https://doi.org/10.1149/1945-7111/ac6d14.

[21] M. Bernt, C. Schramm, J. Schröter, C. Gebauer, J. Byrknes, C. Eickes, H. A. Gasteiger, Effect of the IrO x conductivity on the anode electrode/porous transport layer interfacial resistance in PEM water electrolyzers, J. Electrochem. Soc. 168 (2021) 84513, https://doi.org/10.1149/1945-7111/ac1eb4.

[22] M. Ledendecker, S. Geiger, K. Hengge, J. Lim, S. Cherevko, A.M. Mingers, D. Göhl, G.V. Fortunato, D. Jalalpoor, F. Schüth, C. Scheu, K.J.J. Mayrhofer, Towards maximized utilization of iridium for the acidic oxygen evolution reaction, Nano Res. 12 (2019) 2275–2280, https://doi.org/10.1007/s12274-019-2383-y.

[23] M. Bühler, F. Hegge, P. Holzapfel, M. Bierling, M. Suermann, S. Vierrath, S. Thiele, Optimization of anodic porous transport electrodes for proton exchange membrane water electrolyzers, J. Mater. Chem. A 7 (2019) 26984–26995, https://doi.org/10.1039/C9TA08396K.

[24] S. Brunauer, P.H. Emmett, E. Teller, Adsorption of gases in multimolecular layers, J. Am. Chem. Soc. 60 (1938) 309–319, https://doi.org/10.1021/ja01269a023.

[25] N. Doebelin, R. Kleeberg, Profex: A graphical user interface for the Rietveld refinement program BGMN, J. Appl. Crystallogr. 48 (2015) 1573–1580, https://doi.org/10.1107/S1600576715014685.

[26] A. Jain, S.P. Ong, G. Hautier, W. Chen, W.D. Richards, S. Dacek, S. Cholia, D. Gunter, D. Skinner, G. Ceder, K.A. Persson, Commentary: The materials project: A materials genome approach to accelerating materials innovation, APL Mater. 1 (2013), https://doi.org/10.1063/1.4812323.

[27] A. Fraser, Z. Zhang, G. Merle, J. Gostick, J. Barralet, Powder conductivity assessment using a disposable 3D printed device, Electroanalysis 30 (2018) 1897–1901, https://doi.org/10.1002/elan.201800145.

[28] M. Bernt, H.A. Gasteiger, Influence of ionomer content in IrO 2 /TiO 2 electrodes on PEM water electrolyzer performance, J. Electrochem. Soc. 163 (2016) F3179–F3189, https://doi.org/10.1149/2.0231611jes.

[29] John W. Anthony, Richard A. Bideaux, Kenneth W. Bladh, Monte C. Nichols, Eds., Handbook of Mineralogy, Chantilly, VA 20151-1110, USA.

[30] E.N. Balko, C.R. Davidson, Solid solutions of RuO2 and IrO2, J. Inorg. Nucl. Chem. 42 (1980) 1778–1781, https://doi.org/10.1016/0022-1902(80)80161-8.

[31] E. Padgett, G. Bender, A. Haug, K. Lewinski, F. Sun, H. Yu, D.A. Cullen, A. J. Steinbach, S.M. Alia, Catalyst layer resistance and utilization in PEM electrolysis, J. Electrochem. Soc. 170 (2023) 84512, https://doi.org/10.1149/1945-7111/acee25.

[32] G. Doo, J. Park, J. Park, J. Heo, J. Jung, D.W. Lee, H. Bae, J. Hyun, E. Oh, J. Kwen, K.M. Kim, H.-T. Kim, Contact problems of IrO x anodes in polymer electrolyte membrane water electrolysis, ACS Energy Lett. 8 (2023) 2214–2220, https://doi.org/10.1021/acsenergylett.3c00291.

[33] C.C. Weber, S. de Angelis, R. Meinert, C. Appel, M. Holler, M. Guizar-Sicairos, L. Gubler, F.N. Büchi, Microporous transport layers facilitating low iridium loadings in polymer electrolyte water electrolysis, EES. Catal. 2 (2024) 585–602, https://doi.org/10.1039/D3EY00279A.

[34] F. Hegge, F. Lombeck, E. Cruz Ortiz, L. Bohn, M. von Holst, M. Kroschel, J. Hübner, M. Breitwieser, P. Strasser, S. Vierrath, Efficient and stable low iridium loaded anodes for PEM water electrolysis made possible by nanofiber interlayers, ACS

Appl. Energy Mater. 3 (2020) 8276–8284, https://doi.org/10.1021/acsaem.0c00735.

[35] S.M. Alia, S. Shulda, C. Ngo, S. Pylypenko, B.S. Pivovar, Iridium-based nanowires as highly active Oxygen evolution reaction electrocatalysts, ACS Catal. 8 (2018) 2111–2120, https://doi.org/10.1021/acscatal.7b03787.

[36] L. Li, P. Wang, Z. Cheng, Q. Shao, X. Huang, One-dimensional iridium-based nanowires for efficient water electrooxidation and beyond, Nano Res. 15 (2022) 1087–1093, https://doi.org/10.1007/s12274-021-3603-9.

[37] M.M. Kovács, B. Fritsch, L. Lahn, J. Bachmann, O. Kasian, K.J.J. Mayrhofer, A. Hutzler, D. Dworschak, Electrospun iridium-based nanofiber catalysts for oxygen evolution reaction: Influence of calcination on activity–stability relation, ACS Appl. Mater. Interfaces 16 (2024) 52179–52190, https://doi.org/10.1021/acsami.4c07831.

[38] F. Hu, P. Huang, X. Feng, C. Zhou, X. Zeng, C. Liu, G. Wang, X. Yang, H. Hu, A porous network of boron-doped IrO2 nanoneedles with enhanced mass activity for acidic oxygen evolution reactions, Mater. Horiz. 12 (2025) 630–641, https://doi.org/10.1039/D4MH01358A.

[39] S. Chatterjee, X. Peng, S. Intikhab, G. Zeng, N.N. Kariuki, D.J. Myers, N. Danilovic, J. Snyder, Nanoporous iridium nanosheets for polymer electrolyte membrane electrolysis, Adv. Energy Mater. 11 (2021) 2101438, https://doi.org/10.1002/aenm.202101438.

[40] Q. Dang, H. Lin, Z. Fan, L. Ma, Q. Shao, Y. Ji, F. Zheng, S. Geng, S.-Z. Yang, N. Kong, W. Zhu, Y. Li, F. Liao, X. Huang, M. Shao, Iridium metallene oxide for acidic oxygen evolution catalysis, Nat. Commun. 12 (2021) 6007, https://doi.org/10.1038/s41467-021-26336-2.

[41] Z. Taie, X. Peng, D. Kulkarni, I.V. Zenyuk, A.Z. Weber, C. Hagen, N. Danilovic, Pathway to complete energy sector decarbonization with available iridium resources using ultralow loaded water electrolyzers, ACS Appl. Mater. Interfaces 12 (2020) 52701–52712, https://doi.org/10.1021/acsami.0c15687.

[42] Z. Xie, X. Liang, Z. Kang, Y. Zou, X. Wang, Y.A. Wu, G. King, Q. Liu, Y. Huang, X. Zhao, H. Chen, X. Zou, High-porosity, layered iridium oxide as an efficient, durable anode catalyst for water splitting, CCS Chem (2024) 1–13, https://doi.org/10.31635/ccschem.024.202303586.

[43] M.F. Ernst, V. Meier, M. Kornherr, H.A. Gasteiger, Preparation and performance evaluation of microporous transport layers for proton exchange membrane (PEM) water electrolyzer anodes, J. Electrochem. Soc. 171 (2024) 74511, https://doi.org/10.1149/1945-7111/ad63cf.

[44] P. Lettenmeier, S. Kolb, N. Sata, A. Fallisch, L. Zielke, S. Thiele, A.S. Gago, K. A. Friedrich, Comprehensive investigation of novel pore-graded gas diffusion layers for high-performance and cost-effective proton exchange membrane electrolyzers, Energy Environ. Sci. 10 (2017) 2521–2533, https://doi.org/10.1039/C7EE01240C.

[45] T. Schuler, C.C. Weber, J.A. Wrubel, L. Gubler, B. Pivovar, F.N. Büchi, G. Bender, Ultrathin microporous transport layers: Implications for low catalyst loadings, thin membranes, and high current density operation for proton exchange membrane electrolysis, Adv. Energy Mater. 14 (2024) 2302786, https://doi.org/10.1002/aenm.202302786.

[46] C. Rozain, E. Mayousse, N. Guillet, P. Millet, Influence of iridium oxide loadings on the performance of PEM water electrolysis cells: Part II – Advanced oxygen electrodes, Appl. Catal. B 182 (2016) 123–131, https://doi.org/10.1016/j.apcatb.2015.09.011.

[47] H. Yu, L. Bonville, J. Jankovic, R. Maric, Microscopic insights on the degradation of a PEM water electrolyzer with ultra-low catalyst loading, Appl. Catal. B 260 (2020) 118194, https://doi.org/10.1016/j.apcatb.2019.118194.

[48] C. Liu, M. Shviro, G. Bender, A.S. Gago, T. Morawietz, M.J. Dzara, I. Biswas, P. Gazdzicki, Z. Kang, S.F. Zaccarine, S. Pylypenko, K.A. Friedrich, M. Carmo, W. Lehnert, Degradation effects at the porous transport layer/catalyst layer interface in polymer electrolyte membrane water electrolyzer, J. Electrochem. Soc. 170 (2023) 34508, https://doi.org/10.1149/1945-7111/acc1a5.

[49] Z. Shi, J. Li, J. Jiang, Y. Wang, X. Wang, Y. Li, L. Yang, Y. Chu, J. Bai, J. Yang, J. Ni, Y. Wang, L. Zhang, Z. Jiang, C. Liu, J. Ge, W. Xing, Enhanced acidic water oxidation by dynamic migration of oxygen species at the Ir/Nb2 O5-x catalyst/support interfaces, Angew. Chem. Int. Ed. 61 (2022) e202212341, https://doi.org/10.1002/anie.202212341.

[50] J.Y. Choi, J.G. Kim, H.J. Lee, C. Pak, Advanced iridium catalysts on multi-porous tantalum oxide supports for efficient proton exchange membrane water electrolysis, Int. J. Hydrog. Energy 97 (2025) 57–65, https://doi.org/10.1016/j.ijhydene.2024.11.405.

[51] J.K. Lee, G. Anderson, A.W. Tricker, F. Babbe, A. Madan, D.A. Cullen, J.D. Arregui-Mena, N. Danilovic, R. Mukundan, A.Z. Weber, X. Peng, Ionomer-free and recyclable porous-transport electrode for high-performing proton-exchange-membrane water electrolysis, Nat. Commun. 14 (2023) 4592, https://doi.org/10.1038/s41467-023-40375-x.

[52] M.-G. Kim, H.J. Lee, T.K. Lee, E. Lee, H. Jin, J.-H. Park, S.Y. Cho, S. Lee, H.C. Ham, S.J. Yoo, Iridium selenium oxyhydroxide shell for polymer electrolyte membrane water electrolyzer with low Ir loading, ACS Energy Lett. 9 (2024) 2876–2884, https://doi.org/10.1021/acsenergylett.4c00884.

[53] U. Kuckartz, S. Rädiker, T. Ebert, J. Schehl, Statistik: Eine verständliche Einführung, 2nd ed., Springer VS, Wiesbaden, 2013.

[54] N. Trogisch, A. Hartig-Weiss, H.A. El-Sayed, Limitations of liquid electrolyte RDE experiments for the determination of OER catalyst activity: The effect of the catalyst layer thickness, J. Electrochem. Soc. 171 (2024) 36506, https://doi.org/10.1149/1945-7111/ad2e7f.

[55] T. Lazaridis, B.M. Stühmeier, H.A. Gasteiger, H.A. El-Sayed, Capabilities and limitations of rotating disk electrodes versus membrane electrode assemblies in the investigation of electrocatalysts, Nat. Catal. 5 (2022) 363–373, https://doi.org/10.1038/s41929-022-00776-5.

[56] J. Lopata, Z. Kang, J. Young, G. Bender, J.W. Weidner, S. Shimpalee, Effects of the transport/catalyst layer interface and catalyst loading on mass and charge transport phenomena in polymer electrolyte membrane water electrolysis devices, J. Electrochem. Soc. 167 (2020) 64507, https://doi.org/10.1149/1945-7111/ab7f87.

[57] C. Immerz, M. Paidar, G. Papakonstantinou, B. Bensmann, T. Bystron, T. Vidakovic-Koch, K. Bouzek, K. Sundmacher, R. Hanke-Rauschenbach, Effect of the MEA design on the performance of PEMWE single cells with different sizes, J. Appl. Electrochem. 48 (2018) 701–711, https://doi.org/10.1007/s10800-018-1178-2.

[58] M. Geuß, M. Milosevic, M. Bierling, L. Löttert, D. Abbas, D. Escalera-López, V. Lloret, K. Ehelebe, K.J.J. Mayrhofer, S. Thiele, S. Cherevko, Investigation of iridium-based OER catalyst layers in a GDE half-cell setup: Opportunities and challenges, J. Electrochem. Soc. 170 (2023) 114510, https://doi.org/10.1149/1945-7111/ad07ac.

[59] T.-C. Ma, A. Hutzler, B. Bensmann, R. Hanke-Rauschenbach, S. Thiele, Influence of the Complex Interface between Transport and Catalyst Layer on Water Electrolysis Performance, J. Electrochem. Soc. 171 (2024) 44504, https://doi.org/10.1149/1945-7111/ad3497.

[60] G. Li, M. Xu, Y. Qin, Y. Zhang, Y. Wang, X. Yu, J. Li, Numerical simulation of gradient catalyst layer design in proton exchange membrane water electrolyzer with enhanced performance, Fuel 368 (2024) 131444, https://doi.org/10.1016/j.fuel.2024.131444.

[61] H. Liu, X. Wang, K. Lao, L. Wen, M. Huang, J. Liu, T. Hu, B. Hu, S. Xie, S. Li, X. Fang, N. Zheng, H.B. Tao, Optimizing ionomer distribution in anode catalyst layer for stable proton exchange membrane water electrolysis, Adv. Mater. 36 (2024) e2402780, https://doi.org/10.1002/adma.202402780.

[62] M. Fathi Tovini, A. Hartig-Weiß, H.A. Gasteiger, H.A. El-Sayed, The discrepancy in oxygen evolution Reaction catalyst lifetime explained: RDE vs MEA - dynamicity within the catalyst layer matters, J. Electrochem. Soc. 168 (2021) 14512, https://doi.org/10.1149/1945-7111/abdcc9.

[63] Z. Kang, H. Wang, Y. Liu, J. Mo, M. Wang, J. Li, X. Tian, Exploring and understanding the internal voltage losses through catalyst layers in proton exchange membrane water electrolysis devices, Appl. Energy 317 (2022) 119213, https://doi.org/10.1016/j.apenergy.2022.119213.

[64] M. Mandal, M. Moore, M. Secanell, Measurement of the protonic and electronic conductivities of PEM water electrolyzer electrodes, ACS Appl. Mater. Interfaces 12 (2020) 49549–49562, https://doi.org/10.1021/acsami.0c12111.

[65] E. Hoppe, S. Holtwerth, M. Müller, W. Lehnert, An ex-situ investigation of the effect of clamping pressure on the membrane swelling of a polymer electrolyte water electrolyzer using X-Ray tomography, J. Power Sources 578 (2023) 233242, https://doi.org/10.1016/j.jpowsour.2023.233242.

[66] A. Li, H. Ooka, N. Bonnet, T. Hayashi, Y. Sun, Q. Jiang, C. Li, H. Han, R. Nakamura, Stable potential windows for long-term electrocatalysis by manganese oxides under acidic conditions, Angew. Chem. Int. Ed. 58 (2019) 5054–5058, https://doi.org/10.1002/anie.201813361.

[67] S. Kong, A. Li, J. Long, K. Adachi, D. Hashizume, Q. Jiang, K. Fushimi, H. Ooka, J. Xiao, R. Nakamura, Acid-stable manganese oxides for proton exchange membrane water electrolysis, Nat Catal 7 (2024) 252–261, https://doi.org/10.1038/s41929-023-01091-3.

[68] T. Priamushko, E. Franz, A. Logar, L. Bijelić, P. Guggenberger, D. Escalera-López, M. Zlatar, J. Libuda, F. Kleitz, N. Hodnik, O. Brummel, S. Cherevko, Be aware of transient dissolution processes in Co3O4 acidic oxygen evolution reaction electrocatalysts, J. Am. Chem. Soc. 147 (2025) 3517–3528, https://doi.org/10.1021/jacs.4c14952.

[69] P. Huang, X. Feng, C. Zhou, X. Xu, G. Wang, H. Hu, F. Hu, Na-doped cobalt spinel electrocatalysts prepared by programmed electrostatic spraying for improving OER activity and durability in acidic media, Chem. Eng. J. 500 (2024) 156846, https://doi.org/10.1016/j.cej.2024.156846.

[70] Birk Fritsch, S. Finger, A. Hutzler, BirkFritsch/PEMWE-BioLogic-Analysis: v0.1.0, Zenodo, 2024.